Article

TET2 germline variants promote kidney disease by impairing DNA repair and activating cytosolic nucleotide sensors

Xiujie Liang [1,2,3], Hongbo Liu[1,2,3], Hailong Hu[1,2,3], Eunji Ha [1,2,3], Jianfu Zhou[1,2,3], Amin Abedini [1,2,3], Andrea Sanchez-Navarro [1,2,3], Konstantin A. Klötzer [1,2,3] & Katalin Susztak [1,2,3] ✉

Genome-wide association studies (GWAS) have identified over 800 loci associated with kidney function, yet the specific genes, variants, and pathways involved remain elusive. By integrating kidney function GWAS with human kidney expression and methylation quantitative trait analyses, we identified Ten-Eleven Translocation (TET) DNA demethylase 2 (TET2) as a novel kidney disease risk gene. Utilizing single-cell chromatin accessibility and CRISPR-based genome editing, we highlight GWAS variants that influence *TET2* expression in kidney proximal tubule cells. Experiments using kidney/tubule-specific *Tet2* knockout mice indicated its protective role in cisplatin-induced acute kidney injury, as well as in chronic kidney disease and fibrosis induced by unilateral ureteral obstruction or adenine diet. Single-cell gene profiling of kidneys from *Tet2* knockout mice and *TET2*-knockdown tubule cells revealed the altered expression of DNA damage repair and chromosome segregation genes, notably including *INO80*, another kidney function GWAS target gene itself. Remarkably, both *TET2*-null and *INO80*-null cells exhibited an increased accumulation of micronuclei after injury, leading to the activation of cytosolic nucleotide sensor cGAS-STING. Genetic deletion of cGAS or STING in kidney tubules, or pharmacological inhibition of STING, protected TET2-null mice from disease development. In conclusion, our findings highlight TET2 and INO80 as key genes in the pathogenesis of kidney diseases, indicating the importance of DNA damage repair mechanisms.

Kidney disease is a major global health burden, affecting over 850 million people worldwide[1]. Kidney disease incidence is much higher in older adults[2], and it is one of the fastest-growing causes of mortality[3]. A better understanding of the mechanisms of kidney dysfunction is crucial for developing new therapeutics to treat or cure kidney disease.

Kidney function shows strong heritability[4–6]. Large genome-wide association studies (GWAS) of kidney function have identified more than 800 loci that demonstrate statistically significant and reproducible associations with kidney function[7,8]. However, over 90% of variants identified by GWAS reside in the noncoding regions of the genome[9], which are often correlated due to strong linkage disequilibrium (LD)[10]. Consequently, pinpointing the causal variants, their target genes, specific cell types involved, and underlying disease mechanisms continues to be a major challenge.

[1]Renal, Electrolyte, and Hypertension Division, Department of Medicine, University of Pennsylvania, Perelman School of Medicine, Philadelphia, PA, USA. [2]Penn/CHOP Kidney Innovation Center, Philadelphia, PA, USA. [3]Department of Genetics, University of Pennsylvania, Perelman School of Medicine, Philadelphia, PA, USA. ✉e-mail: ksusztak@pennmedicine.upenn.edu

Disease-causing variants are often located in cell type-specific regulatory regions, potentially altering the binding strength of transcription factors and resulting in quantitative differences in the expression of cell type-specific target genes[9]. Expression quantitative trait loci (eQTL) analysis, which defines the association between genetic variants and tissue gene expression, has been widely used to identify target genes in GWAS[4,11–13]. Analyzing the effects of genotype on the epigenome, such as DNA methylation, can improve gene and cell type prioritization[8]. In addition, examining changes in gene expression and regulation at the single-cell level, rather than at the whole tissue bulk level, is critical[9]. While computational integration strategies have prioritized new kidney function risk genes based on GWAS and human kidney multi-omics datasets, these studies require careful follow-up cell and animal model experiments to substantiate the causal role of a specific gene[8].

DNA methylation, the addition of a methyl group to the 5-position of cytosines, is mediated by DNA methyltransferases (DNMTs)[14]. The Ten-Eleven Translocation (TET) enzymes play a role in demethylation by converting 5-methylcytosine (5mC) to 5-hydroxymethylcytosine (5hmC), 5-formylcytosine, and 5-carboxylcytosine[15,16]. DNA methylation is an energetically costly process which also increases the mutation rate, as 5mC is converted to thymine, which is difficult to repair[17]. DNA methylation is an important regulator of multiple DNA-based processes. Most studies have analyzed the role of cytosine methylation in gene expression regulation[14]. Cytosine methylation renders the DNA region less accessible to the transcriptional machinery by recruiting methyl binding proteins and altering transcription factor binding strength[18]. Cytosine methylation is critical during kidney development and our previous studies demonstrated the key role of *Dnmt1* in Six2 in progenitor cells as it is required for transposable element silencing[19] while *Dnmt3a* and *Dnmt3b* are essential for the silencing developmental genes[20]. Kidneys obtained from patients with chronic kidney disease (CKD and fibrosis) also showed important changes in cytosine methylation at more than 100 CpG sites[21]. Globally, more CpG sites show higher methylation level in CKD[21]. These methylation changes correlate and predict kidney function decline, indicating their potential role in disease development[21].

DNA damage occurs in various forms, including abasic sites, adducts, DNA-protein cross-links, insertion/deletion mismatches, double-strand breaks (DSBs), and single-strand breaks (SSBs)[22]. Cells respond to DNA damage by initiating a series of highly coordinated events to repair DNA, known as the DNA damage response (DDR), which includes base excision repair (BER), nucleotide excision repair (NER), mismatch repair (MMR), non-homologous end joining (NHEJ), and homologous recombination (HR)[22]. The ataxia teleangiectasia mutated (ATM) and ATM-RAD3 related (ATR), and the DNA-dependent protein (DNA-PK) are three kinases that control DDR and orchestrate DSB[22]. In cases where the DNA damage exceeds the repair capacity of the cell, the DDR triggers senescence or apoptosis[22]. By arresting proliferation and promoting clearance of damaged cells, the DDR acts as a barrier to tumorigenesis[23]. Recent studies highlighted the role of ATM and ATR in kidney disease development[24,25]. Mutations in DNA repair pathway genes, such as *ERCC1*, *ERCC2*, *ERCC6*, and *ERCC8*, have been associated with progeria, cancer, or immunodeficiency[24]. The modified *ERCC1* knockout mouse model, which expresses a liver-specific *ERCC1* rescue transgene, developed proteinuria, segmental glomerulosclerosis, and end-stage renal failure[24,25]. The role of cytosine methylation in DDR is not fully understood; however, both epigenetic changes and DNA damage are strongly associated with aging[26].

In this study, we identified genetic variants associated with kidney function that concurrently lower the expression of *Tet2* in kidney proximal tubule cells. Kidney/tubule-specific gene knockout mice have highlighted the protective roles of *Tet2* both in acute kidney injury and chronic fibrosis. Molecular studies indicated the role of *TET2* in the HR pathway for DSB repair and in ensuring proper chromosome segregation in proximal tubule cells. Loss of *Tet2* lead to kidney injury by leaving micronuclei in the cytosol, resulting in cGAS-STING activation and subsequent kidney disease development.

Results

Prioritization of *TET2* for kidney function

Multiple genome-wide association studies have recognized common noncoding nucleotide variants on chromosome 4 associated with kidney function[5,8,27–29]. To identify the causal variants within this locus, we performed statistical fine mapping using the SuSie method. We identified two credible sets: rs6533181 (posterior inclusion probability, PIP = 9.98×10^{-8}), rs115918101 (PIP = 8.82×10^{-8}), and rs2214407 (PIP = 3.54×10^{-8}) (Fig. 1a). The variant rs6533181 was strongly and significantly associated with kidney function in the eGFR creatinine GWAS ($P = 1.41 \times 10^{-10}$) (Fig. 1b). The minor allele frequency (MAF) of the variant rs6533181 was 0.3397.

To further dissect this region, we integrated the GWAS data with kidney methylation quantitative trait loci (meQTLs) and expression quantitative trait loci (eQTLs) analyses. We observed a significant association between the variant rs6533181 and CpG methylation (kidney cg11878490 meQTLs, $P = 1.29 \times 10^{-19}$) and *TET2* expression in kidney samples (eQTL, $P = 1.19 \times 10^{-3}$) (Fig. 1b, c). Multi-tissue eQTL analysis from the GTEx project (Genotype-Tissue Expression) indicated that rs6533181 is associated with *TET2* expression levels also in the skin ($P = 1.2 \times 10^{-10}$) and in fibroblasts ($P = 6.1 \times 10^{-5}$).

To test whether eGFR, cytosine methylation of cg11878490, and *TET2* expression share causal variants at this locus, we performed a statistical colocalization analysis using Moloc. We found compelling evidence that the variants linked with kidney function, CpG methylation, and TET2 expression in the kidney tubule (allele-specific expression analysis, ASE) were shared, as indicated by a high posterior probability (ASE.PP.H4.abf = 0.87). TET2 expression in kidney tubules (613 tubule samples) was strongly genotype-dependent (rs6533181, eGFR GWAS risk allele T, ASE $P = 9.7 \times 10^{-5}$) (Fig. S1a). The association score in the combined SNP-to-gene (cS2G) linking strategy[30] for *TET2* was 1, strongly suggesting that *TET2* is the target gene of this genetic locus.

Considering that SNPs located in the regulatory region are more likely to be causal[31], we employed our human kidney single-nuclear assay for transposase-accessible chromatin sequencing (snATAC-seq) to further prioritize risk variants. The variant rs6533181 was not located in an open chromatin region in the human kidney (Fig. S1b). However, rs1541374 and rs7661349, which are in very strong linkage disequilibrium (LD) with rs6533181 ($r > 0.93$ and $r > 0.98$, respectively), were located within an open chromatin region in the proximal tubule cell and the promoter region of TET2 (Fig. 1d). Variant rs1541374 showed the strongest association with kidney function in the eGFR creatinine GWAS ($P = 8.63 \times 10^{-11}$) (Fig. S2a). rs7661349 was also significantly associated with kidney function in the eGFR creatinine GWAS ($P = 4.02 \times 10^{-9}$) (Fig. S2b). We found a significant association between the variants rs1541374 and rs7661349 and CpG methylation (cg11878490 meQTLs, $P = 2.98 \times 10^{-18}$ and $P = 1.58 \times 10^{-20}$, respectively) (Fig. S2a–d). The MAFs of rs1541374 and rs7661349 are 0.3172 and 0.3357, respectively. We observed a significant association between the variant rs1541374 and *TET2* expression in kidney tubule samples (kidney tubule eQTL, $P = 5.08 \times 10^{-4}$) (Fig. S2a) and a significant association between the variant rs7661349 and *TET2* expression in kidney samples (kidney eQTL, $P = 1.20 \times 10^{-3}$) (Fig. S2b). Allele-specific expression (ASE) analysis for rs1541374 showed that *TET2* expression in kidney tubules was strongly genotype-dependent (rs1541374, eGFR GWAS risk allele T, ASE $P = 8.3 \times 10^{-3}$) (Fig. S2e). TET2 expression in kidney tubules was also strongly genotype-dependent for rs7661349 (eGFR GWAS risk allele T, ASE $P = 2.2 \times 10^{-4}$) (Fig. S2f). These observations prompted us to hypothesize that rs7661349 and rs1541374 are the likely causal variants. To demonstrate that rs1541374 and
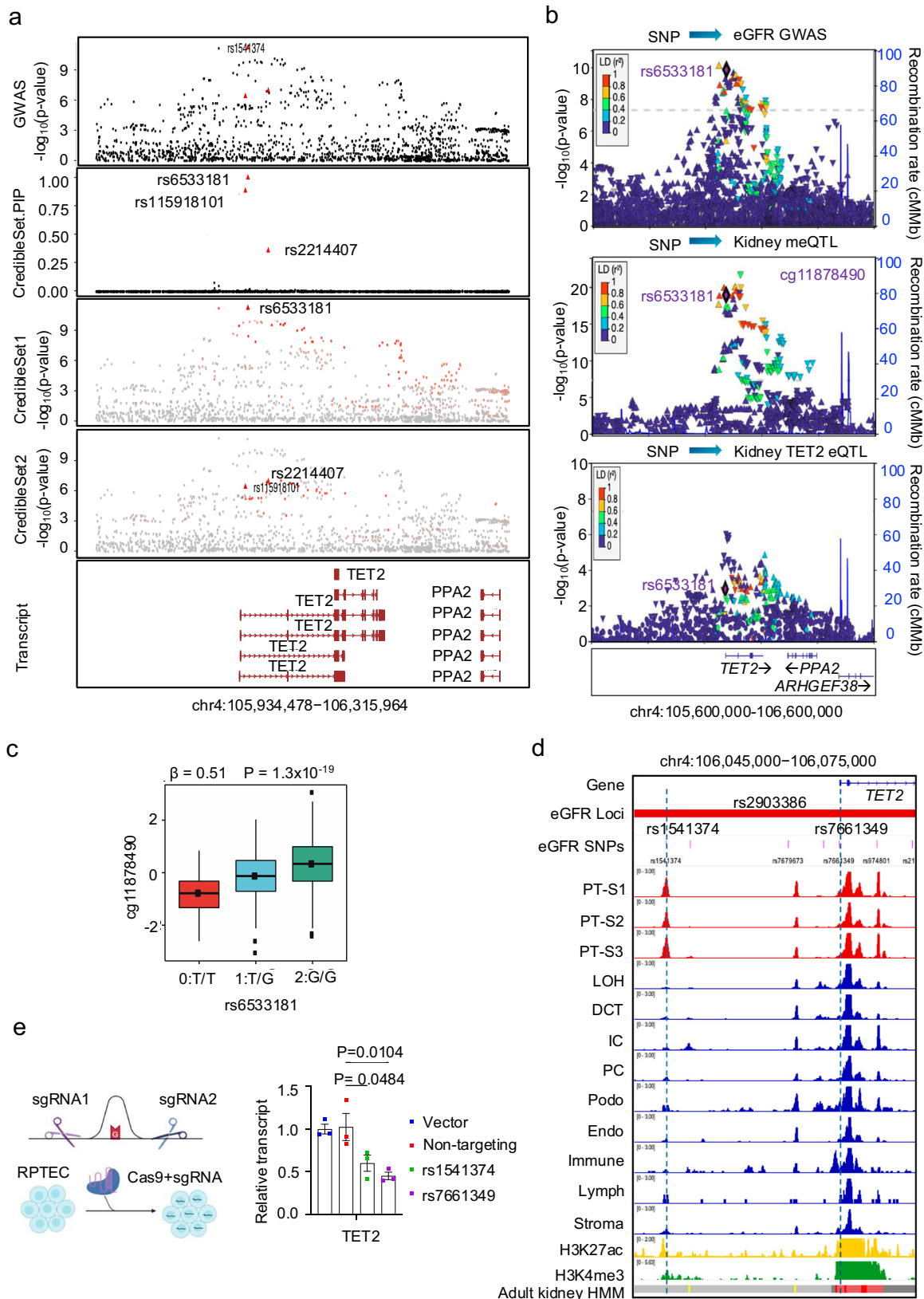
rs7661349 regulate the expression of *TET2* in human kidney proximal tubule cells, we performed CRISPR-based deletion of the open chromatin region containing these two variants (Figs. 1e and S3a). Deletion of rs1541374 and rs7661349, but not of the non-target regions, lowered *TET2* levels, but not *Inorganic pyrophosphatase 2* (*PPA2*) levels (Figs. 1e and S3b).

Our human kidney single-nuclear RNA sequencing (snRNA-seq) data showed that *TET2* expression in the proximal tubule (S3 segment) was lower in diseased kidneys compared to healthy kidneys (Fig. S4a). Immunofluorescence staining further confirmed that the protein level of TET2 in the proximal tubule was lower in diseased kidneys compared to controls (Fig. S4b).

Fig. 1 | Identification of *TET2* as a kidney disease risk gene. a LocusZoom plots of eGFR GWAS (genotype and eGFRcrea association, $n = 1,746,932$) and fine mapping for chr4: 105,934,478-106,315,964. Each dot represents a SNP, with color indicating LD association. **b** LocusZoom plots of eGFR GWAS (genotype and eGFRcrea association, $n = 2.2M$), kidney CpG cg11878490 meQTL (genotype and cg11878490 methylation association, $n = 443$), and kidney *TET2* eQTLs (genotype and *TET2* expression association, $n = 686$)[8]. The y-axis displays the -log10 (*p*-values) of association tests from GWAS, meQTL, and eQTLs studies. **c** Genotype (rs6533181, x-axis) and normalized CpG methylation (cg11878490, y-axis) in human kidneys ($n = 443$). The effect size (Beta) is 0.51. Center line represents the median, the box limits show 25th and 75th percentiles, and whiskers extend to 5th and 95th percentiles. *P*-value was derived from linear regression meQTL model. **d** From top: Gene browser view of the eGFR GWAS SNPs in the specified regions; single-nucleus Assay for

Transposase-Accessible Chromatin using sequencing (snATAC-seq) analysis of chromatin accessibility of human kidneys, including S1, S2, and S3 segments of the proximal tubules (PT-S1, PT-S2, PT-S3), loop of Henle (LOH), distal convoluted tubule (DCT), connecting tubule (CNT), intercalated cells (IC), collecting duct principal cell types (PC), podocytes (Podo), endothelial cells (Endo), immune cells (Immune), lymphocyte (Lymph). Human kidney histone modifications by chromatin immunoprecipitation (ChIP-seq) and chromatin states are also shown. **e** Relative transcript levels of *TET2* after CRISPR-mediated deletion of the locus, with a sample size of $n = 3$. *GAPDH* was used for normalization. Data are shown as mean ± SEM and were analyzed using one-way ANOVA followed by Tukey's post hoc test for multigroup comparison. The diagram was created with BioRender.com. Source data are provided as a Source Data file.

In summary, by integrating kidney function GWAS, single-nucleus epigenome mapping, and CRISPR-Cas9 gene editing, we identified *TET2* as a risk gene for kidney disease, specifically within kidney proximal tubule cells, where lower *TET2* expression was associated with an elevated risk of renal disease.

Kidney-specific *Tet2* knockout mice show increased severity of acute and chronic kidney disease

To study the role of *TET2* in kidney disease development, we generated mice with genetically lowered *Tet2* expression in kidney cells by breeding *Six2^Cre^* mice with *Tet2^f/f^* mice[32]. Gene expression analysis confirmed the reduction in *Tet2* expression in the proximal tubules of the kidneys in adult *Six2^Cre^Tet2^f/f^* mice compared to *Six2^Cre^* mice (Fig. S5a, b). *Six2^Cre^Tet2^f/f^* mice were born at the expected Mendelian ratio, appeared healthy at birth, and showed no significant differences in life span at 40 weeks of age[32]. Next, we analyzed *Six2^Cre^Tet2^wt/f^* and *Six2^Cre^Tet2^f/f^* mice in a cisplatin-induced acute kidney injury (AKI) model (Fig. 2a). Blood urea nitrogen (BUN) levels were elevated in cisplatin-injected *Six2^Cre^Tet2^wt/f^* and *Six2^Cre^Tet2^f/f^* mice compared to cisplatin-injected *Six2^Cre^* mice (Fig. 2b). Histological analysis indicated more hyaline casts, loss of brush border, and tubular lumen dilation in kidneys of cisplatin-injected *Six2^Cre^Tet2^wt/f^* and *Six2^Cre^Tet2^f/f^* mice compared to those in cisplatin-injected control mice (Fig. 2c). Expression levels of kidney injury markers, such as *kidney injury molecule 1* (*Kim1*) and *neutrophil gelatinase-associated lipocalin* (*Ngal*), were higher in kidneys of cisplatin-injected *Six2^Cre^Tet2^wt/f^* and *Six2^Cre^Tet2^f/f^* mice when compared with cisplatin-injected control *Six2^Cre^* mice (Fig. 2d).

To understand the role of *TET2* in kidney fibrosis, we subjected both control and *Six2^Cre^Tet2^f/f^* mice to unilateral ureteral obstruction (UUO) injury (Fig. 2e) and analyzed their phenotypes in an adenine diet-induced chronic kidney fibrosis model (Fig. 2j). Histological examination revealed more severe kidney fibrosis, including more dilated tubules with or without proteinaceous casts, increased immune cell infiltration, and loss of brush border in the kidneys of UUO surgery or adenine-diet-subjected *Six2^Cre^Tet2^f/f^* mice compared with those in UUO/adenine-subjected *Six2^Cre^* mice (Fig. 2f, l). Sirius Red staining indicated elevated profibrotic collagen deposition in the kidneys of *Six2^Cre^Tet2^f/f^* mice subjected to UUO surgery compared to kidneys of UUO/adenine-subjected control *Six2^Cre^* mice (Fig. 2g,m). Expression of fibrosis markers (*Fibronectin 1*, *Collagen1a1*, and *Collagen3a1*) was higher in the kidneys of UUO/adenine-subjected *Six2^Cre^Tet2^f/f^* mice compared to *Six2^Cre^* mice with UUO surgery (Fig. 2h, n) and inflammation markers (*Interleukin 6*, *C-C motif chemokine ligand 2*, and *Vascular cell adhesion molecule 1*) were as higher in kidneys of UUO-subjected *Six2^Cre^Tet2^f/f^* mice compared to kidneys of UUO-subjected *Six2^Cre^* mice (Fig. 2h). Protein expression analysis by immunoblotting further confirmed that fibronectin1 and aSMA expressions were prominently increased in kidneys of UUO/adenine-subjected *Six2^Cre^Tet2^f/f^* mice compared to UUO-subjected *Six2^Cre^* mice (Fig. 2i, o).

As *Six2* is expressed during kidney development[33], we generated mice with a conditional, inducible genetic deletion of *Tet2* in tubule cells by crossing *Pax8^rtTA^* mice and *TRE^Cre^* mice with *Tet2^f/f^* mice (Fig. 3a). Gene expression analysis confirmed the reduction in *Tet2* expression in the kidneys of *Pax8^rtTA^TRE^Cre^Tet2^f/f^* mice compared to *Tet2^f/f^* mice (Fig. 3b). We observed that *Pax8^rtTA^TRE^Cre^Tet2^f/f^* mice were born at the expected Mendelian ratio and appeared healthy at birth, and we observed no differences in life span at 40 weeks of age. Most importantly, the kidneys of *Pax8^rtTA^TRE^Cre^Tet^wt/f^* mice or *Pax8^rtTA^TRE^Cre^Tet2^f/f^* mice injected with cisplatin showed more severe injury, including changes in kidney injury biomarkers, gene expression, and structural damage, compared to those in the control *Tet2^f/f^* mice injected with cisplatin (Fig. 3d–f).

In summary, our data indicate that tubule-specific *Tet2* loss exacerbates kidney dysfunction in both AKI and CKD.

Tet2 deficiency in tubule cells caused chromosome missegregation and accumulation of micronuclei

To investigate the mechanisms by which *Tet2* loss in tubule cells contributes to more severe kidney injury, we performed droplet-based snRNA-seq on kidney samples from wild-type (WT) and *Six2^Cre^Tet2^f/f^* mice at baseline and following UUO injury (Fig. 4a). Following sequencing and alignment, we identified 38,714 high-quality cells. Subsequently, we applied dimensionality reduction using uniform manifold approximation and projection (UMAP) and graph-based clustering (Figs. 4b, c, and S6a). This analysis recognized 19 distinct clusters (Figs. 4b, c, and S6a), which were annotated based on the expression of previously published gene markers (Fig. 4b)[34]. *Tet2* level was markedly lower in *Six2^Cre^Tet2^f/f^* mice (Fig. S6c). We found that *Tet2* is mainly expressed in the proximal straight tubule (PST) (Fig. S6b) which was consistent with the in situ hybridization (ISH) and immunofluorescence (IF) staining data.

We next identified 2,218 differentially expressed genes (DEGs) in PST cells in kidneys from UUO-subjected *Six2^Cre^Tet2^f/f^* mice compared to UUO-subjected control mice kidneys (with an adjusted *p*-value < 0.05). Pathway analysis revealed significant enrichment in pathways related to metabolic processes, cell differentiation, and chromosome organization and segregation processes (Fig. 4d).

To complement the mouse kidney analysis, we performed RNA sequencing (RNA-seq) analysis on control and *TET2* knockdown (KD) human renal proximal tubule epithelial cells (RPTECs) (Fig. 4e). We generated these cells by transducing RPTECs, which stably express dCas9-ZIM3-KRAB, with either non-targeting control sgRNA or sgRNA targeting *TET2* (Fig. 4e). We identified over 2000 genes, including *TET2* (Figs. 4f and S6), with a reduction of more than 30% in *TET2* KD RPTECs compared to control cells. Pathway analysis of these differentially expressed genes showed enrichment in processes related to nuclear division, mitotic cell cycle, and chromosome segregation (Fig. 4g). We identified 45 genes involved in the chromosome segregation process, which were dramatically lowered in *TET2* KD cells, including *INO80* and *EME1* (Supplementary Data 1).
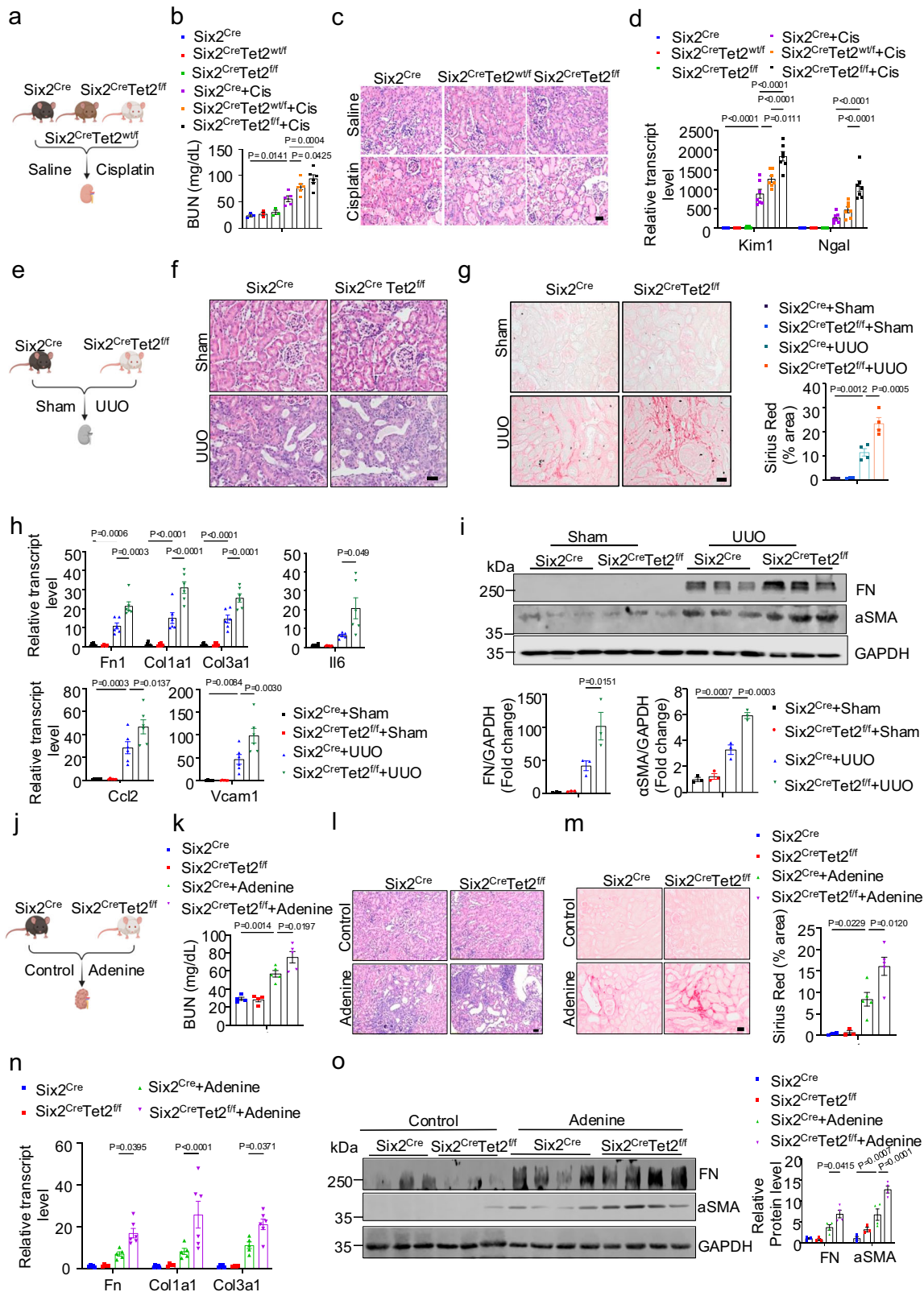
To confirm the role of *Tet2* in chromosome segregation in tubule cells, we next conducted in vitro studies by isolating primary tubule cells from the kidneys of *Six2^Cre* control mice and *Six2^CreTet2^{f/f}* mice (Fig. 4h), both in the presence and absence of doxorubicin, a DNA-intercalating agent (Fig. 4h)[35]. We observed various types of chromosome segregation errors in doxorubicin-treated primary tubule cells

isolated from kidneys of *Six2^CreTet2^{f/f}* mice compared to control cells (Fig. 4i), including micronuclei formation[36,37]. There were more micronuclei in doxorubicin-treated tubule cells isolated from kidneys of *Six2^CreTet2^{f/f}* mice compared to those from kidneys of *Six2^Cre* mice (Fig. 4k). Similar results were obtained from control and *TET2* knock-down human RPTECs treated with doxorubicin (Fig. 4j, l).

Fig. 2 | Tubule-specific *Tet2* loss exacerbated renal injury and fibrosis.
a Experimental design. *Six2^Cre*, *Six2^cre^Tet2^wt/f*, and *Six2^cre^Tet2^f/f* mice were injected with saline or cisplatin and euthanized 3 days later. Created with BioRender.com. **b** BUN levels were measured in *Six2^Cre*, *Six2^cre^Tet^wt/f*, and *Six2^cre^Tet2^f/f* mice injected with saline (*n* = 3) or cisplatin (*Six2^Cre* *n* = 5, *Six2^cre^Tet^wt/f* *n* = 6, *Six2^cre^Tet2^f/f* *n* = 6).
c Representative images of H&E-stained kidneys sections from *Six2^Cre* and *Six2^cre^Tet2^f/f* mice injected with saline or cisplatin. **d** Relative transcript level of *Kim1* and *Ngal* in kidneys of *Six2^Cre*, *Six2^cre^Tet^wt/f*, and *Six2^cre^Tet2^f/f* mice injected with saline or cisplatin. *Gapdh* was used for normalization. Saline-injected group: *Six2^Cre* (*n* = 6), *Six2^cre^Tet^wt/f* (*n* = 4), and *Six2^cre^Tet2^f/f* (*n* = 6). Cisplatin-injected groups: *n* = 7 each.
e Experimental setup. *Six2^Cre* and *Six2^cre^Tet2^f/f* mice underwent sham-operation or unilateral ureteral obstruction (UUO) and were euthanized 4 days post-surgery. Created with BioRender.com. **f** Representative images of H&E-stained kidney sections from *Six2^Cre* and *Six2^cre^Tet2^f/f* mice subjected to sham-operation or UUO surgery. **g** Representative images of Sirius Red-stained kidney sections with quantification from *Six2^Cre* and *Six2^cre^Tet2^f/f* mice subjected to sham-operation or UUO surgery. Sham-operated group: *Six2^Cre* (*n* = 4) and *Six2^cre^Tet2^f/f* (*n* = 3); UUO-operated groups: *n* = 4 each. **h** Relative transcript levels of *Fibronectin1* (*Fn1*), *Collagen1a1* (*Col1a1*), *Collagen1a1* (*Col3a1*), *Interleukin 6* (*Il6*), *C-C motif chemokine ligand 2* (*Ccl2*), and *Vascular cell adhesion molecule 1* (*Vcam1*) in kidneys of *Six2^Cre*

and *Six2^cre^Tet2^f/f* mice after sham-operation or UUO surgery (*n* = 6 per group).
i Representative Western blots and densitometric quantification of FN and alpha-smooth muscle (aSMA) in kidneys of *Six2^Cre* and *Six2^cre^Tet2^f/f* mice subjected to sham-operation or UUO surgery (*n* = 3 biological replicates). **j** Experimental design for adenine-induced chronic kidney disease model. *Six2^Cre* and *Six2^cre^Tet2^f/f* mice were placed on control or adenine diet for 4 weeks. Created with BioRender.com. **k** Serum BUN levels in *Six2^Cre* and *Six2^cre^Tet2^f/f* mice on control (*n* = 4) or adenine diets (*n* = 5). **l** Representative images of H&E-stained kidney sections from *Six2^Cre* and *Six2^cre^Tet2^f/f* mice on control or adenine diet. **m** Representative images of Sirius Red-stained kidney sections with quantification from *Six2^Cre* and *Six2^cre^Tet2^f/f* mice on control (*n* = 3) or adenine diet (*n* = 5). **n** Relative transcript levels of *Fn1*, *Col1a1*, and *Col3a1* in kidneys of *Six2^Cre* and *Six2^cre^Tet2^f/f* mice on a control diet (*Six2^Cre*: *n* = 5; *Six2^cre^Tet2^f/f*: *n* = 4) or adenine diet (*Six2^Cre*: *n* = 5; *Six2^cre^Tet2^f/f*: *n* = 6). **o** Representative Western blots and densitometric quantification of FN and aSMA in kidneys of *Six2^Cre* and *Six2^cre^Tet2^f/f* mice on a control diet (*n* = 3 per group) or an adenine diet (*n* = 4 per group). Scale bar = 20 μm. Data are presented as mean ± SEM and were analyzed using one-way ANOVA followed by Tukey's post hoc test (b, d, g-i, k, m-o). Data are representative of three independent experiments (**c,f,l**). Source data are provided as a Source Data file.
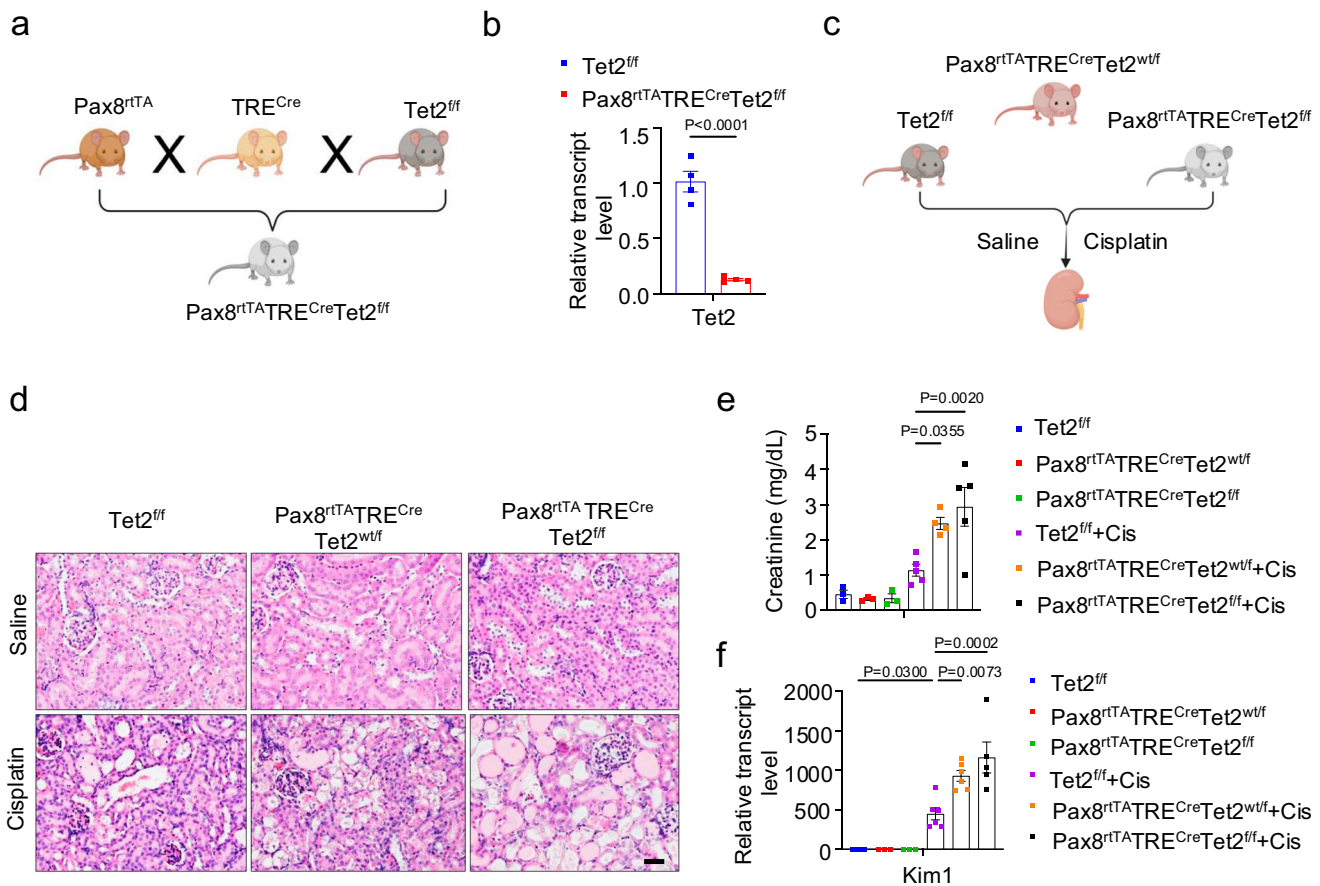
Fig. 3 | Tubule-specific *Tet2* deficiency exacerbates cisplatin-induced kidney injury. **a** Experimental scheme for the generation of *Pax8^rtTA^Cre^TRE^Tet2^f/f* mice. Created with BioRender.com. **b** Relative transcript levels of *Tet2* in kidneys of control and *Pax8^rtTA^Cre^TRE^Tet2^f/f* mice. Each group contains *n* = 4 biological replicates. **c** Experimental design. *Tet2^f/f*, *Pax8^rtTA^Cre^TRE^Tet2^wt/f*, and *Pax8^rtTA^Cre^TRE^Tet2^f/f* mice were injected with saline or cisplatin for 3 days. Created with BioRender.com. **d** Representative images of H&E-stained kidney sections from *Tet2^f/f*, *Pax8^rtTA^Cre^TRE^Tet2^wt/f*, and *Pax8^rtTA^Cre^TRE^Tet2^f/f* mice, injected with saline or cisplatin. Scale bar = 20 μm. Data are representative of three independent experiments. **e** Serum creatinine levels in *Tet2^f/f*, *Pax8^rtTA^Cre^TRE^Tet2^wt/f*, and *Pax8^rtTA^Cre^TRE^Tet2^f/f* mice

injected with saline or cisplatin. In the saline-injected groups: *n* = 3 each for each genotype. In the cisplatin-injected groups: *Tet2^f/f*: *n* = 5, *Pax8^rtTA^Cre^TRE^Tet2^wt/f*: *n* = 4, *Pax8^rtTA^Cre^TRE^Tet2^f/f*: *n* = 5. **f** Relative transcript levels of *Kim1* in kidneys of *Tet2^f/f*, *Pax8^rtTA^Cre^TRE^Tet2^wt/f*, and *Pax8^rtTA^Cre^TRE^Tet2^f/f* mice injected with saline or cisplatin. Saline-injected groups: *n* = 3 for each genotype. In the cisplatin-injected groups: *Tet2^f/f*: *n* = 6, *Pax8^rtTA^Cre^TRE^Tet2^wt/f*: *n* = 6, *Pax8^rtTA^Cre^TRE^Tet2^f/f*: *n* = 5. Data are presented as mean ± SEM and were analyzed using analyzed using a two-tailed unpaired Student's t-test (**b**) or a one-way ANOVA followed by Tukey's post hoc test for multigroup comparison (e-f). Source data are provided as a Source Data file.
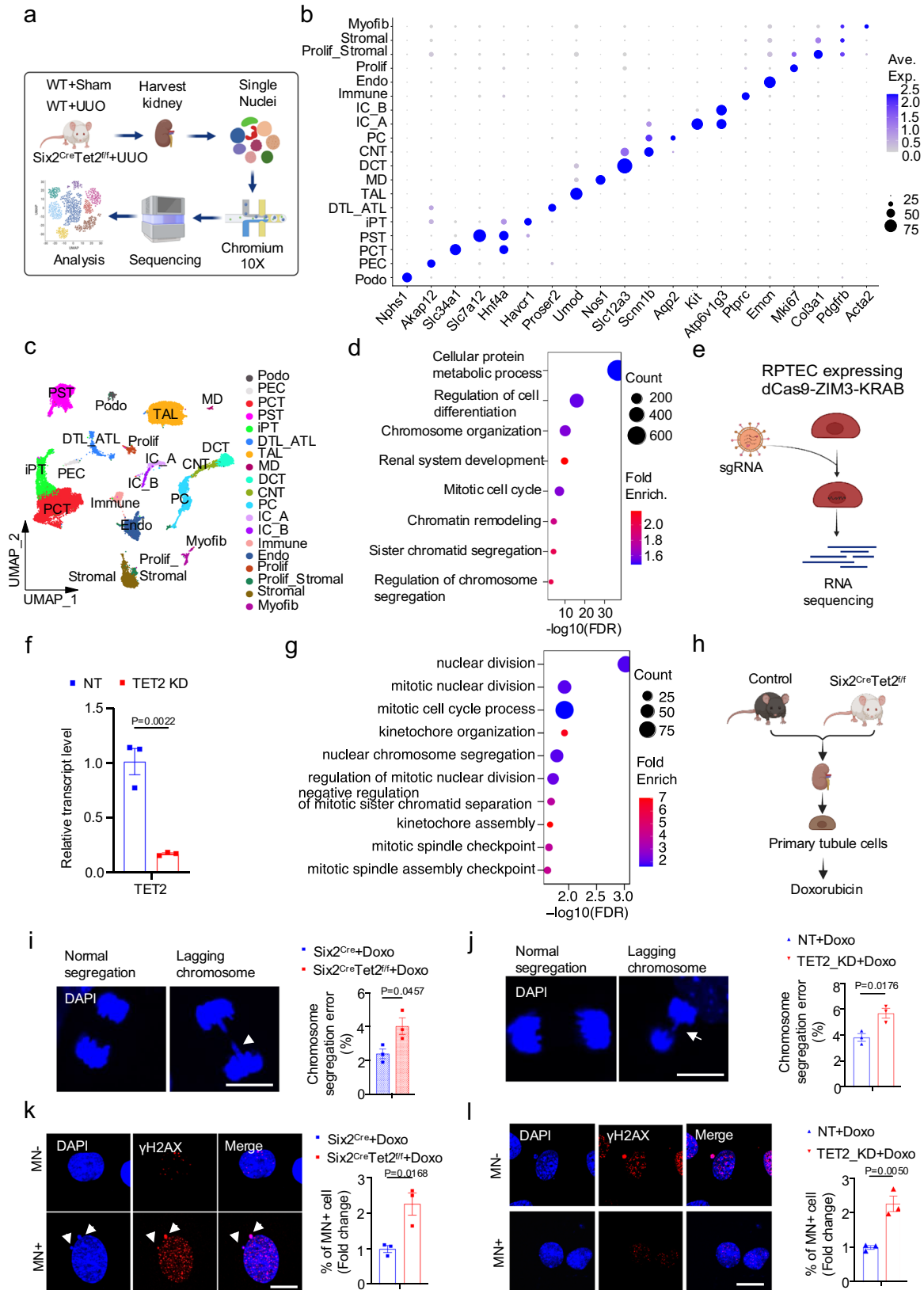
In summary, our unbiased gene expression and experimental analyses underscored the critical role of TET2 in chromosome segregation and prevention of micronuclei accumulation within kidney tubule cells.

Loss of *Tet2* in proximal tubule cell was associated with greater DNA damage due to the impairment in DNA damage repair

Next, we analyzed RNA-seq data from a substantial collection ($n > 400$) of control and diseased human kidney samples. We focused on genes

Fig. 4 | *Tet2* loss was associated with chromosome segregation defect and an increase in cytosolic micronuclei. a This diagram summarizes nuclear isolation and single-nucleus RNA sequencing (snRNA-seq) of kidneys from wild type (WT) control and *Six2^{Cre}Tet2^{f/f}* mice subjected to sham-operation or UUO surgery, using the 10X Genomics platform. Created with BioRender.com. **b** Bubble plots show representative marker gene expression across 19 cell clusters: Podocyte (Podo), Parietal epithelial cells (PEC), Proximal convoluted tubule (PCT), Proximal straight tubule (PST), Injured proximal tubule (iPT), Descending and ascending thin limb of loop of Henle (DTL_ATL), Thick ascending limb (TAL), Macula densa (MD), Distal convoluted tubule (DCT), Connecting tubule (CNT), Principal cells (PC), Type A and Type B intercalated cells of collecting duct (IC_A and IC_B), Endothelial cells (Endo), Proliferating cells (Prolif), Proliferating stromal (Prolif_Stromal), Myofibroblast (Myofib). The bubble size represents the percentage of positive cells, and color intensity indicates expression level. **c** UMAP dimension reduction of snRNA-seq from WT control and *Six2^{Cre}Tet2^{f/f}* mice subjected to sham-operation or UUO surgery. **d** Gene Ontology (GO) functional analysis of differentially expressed genes (DEGs) observed in control WT and *Six2^{Cre}Tet2^{f/f}* mice after UUO surgery. Enriched biological process (*p* < 0.05) are shown, with *p*-values transformed to −log10.

Bubble size indicates gene count, and color shows fold change. **e** This diagram summarizes the RNA sequencing (RNA-seq) process for control and *TET2* knockdown RPTEC (CRISPR). Created with BioRender.com. **f** Relative *TET2* transcript levels in control and knockdown RPTEC (*n* = 3 biological replicates per group). **g** GO analysis of genes with > 30% reduced expression in *TET2* knockdown RPTEC compared to control cells. Enriched terms (*p* < 0.05) are log-transformed. **h** Experimental design for primary tubule cells from control and *Six2^{Cre}Tet2^{f/f}* mice treated with doxorubicin. Created with BioRender.com. **i,j** DAPI staining shows chromosome segregation in control and *Tet2*-knockout primary tubule cells or *TET2* knockdown RPTEC. Right panel: Quantifications of doxorubicin-treated cells with chromosome segregation defect (*n* = 3 biological replicates per group). **k,l** Representative images of γH2AX and DAPI staining, showing primary tubule cells or RPTEC with or without micronuclei. Right panel: Quantifications of the doxorubicin-treated cells with micronuclei. Each group contains *n* = 3 biological replicates. Scale bar = 20 μm. Data are presented as mean ± SEM, analyzed with two-tailed unpaired Student's t-test (**f,i**–**l**). Source data are provided as a Source Data file.

whose levels strongly correlated with *TET2*. We identified 160 genes, all with a false discovery rate (*FDR*) < 0.05, that correlated with *TET2* expression. Gene ontology analysis indicated strong enrichment for genes playing a role in DNA DSB repair via homologous recombination (HR) (Supplementary Data 2). DNA DSBs are highly cytotoxic and must be repaired to maintain chromosomal integrity[22,38]. To investigate the effects of *Tet2* loss on DNA damage in tubule cells, we measured DSB marker γH2AX level in cells treated with or without doxorubicin. We observed that γH2AX level was higher in doxorubicin-treated cells isolated from kidneys of *Six2^{Cre}Tet2^{f/f}* mice when compared to doxorubicin-treated cells isolated from kidneys of control mice (Fig. 5a). The protein level of γH2AX was also elevated in kidneys of cisplatin-injected *Six2^{Cre}Tet2^{f/f}* mice or *Six2^{Cre}Tet2^{f/f}* mice operated with UUO surgery when compared to control cisplatin-injected mice or mice with UUO surgery (Fig. 5b).

Altered DNA damage response (DDR) during mitosis can lead to the accumulation of damaged DNA and chromosome mis-segregation[35,39]. We observed higher levels of phosphorylated ataxia telangiectasia mutated kinase (p-ATM), phosphorylated checkpoint kinase 2 (p-CHK2), and phosphorylated p53 (pp53), which are markers of the DDR that response to DSB, in doxorubicin-treated cells isolated from the kidneys of *Six2^{Cre}Tet2^{f/f}* mice when compared with those in doxorubicin-treated control cells isolated the kidneys of control mice (Fig. 5c, d). Similarly, the expression of phosphorylated ataxia telangiectasia and Rad3-related kinase (p-ATR) and phosphorylated checkpoint kinase 1 (p-CHK1), which are critical for the DNA SSBs, was elevated (Fig. S8a). Additionally, we observed higher levels of γH2AX and p-p53 in cells with rs1541374 or rs7661349 deletions compared to cells with non-target region deletions (Fig. S8b). These results are consistent with the observation of increased DNA damage and pronounced chromosome segregation errors in tubule cells lacking *Tet2*, underlining the critical role of Tet2 in maintaining genomic stability.

Unresolved DNA damage may cause cell cycle arrest and apoptosis[22]. We observed that the level of cleaved caspase 3; a marker of apoptosis, was higher in the doxorubicin-treated primary tubule cells isolated from the kidneys of *Six2^{Cre}Tet2^{f/f}* mice compared with those from doxorubicin-treated control (WT) cells (Fig. S8c). Additionally, we observed an increase in both cleaved caspase-3 levels and the number of TUNEL-positive cells, which are indicative of apoptosis, in the kidneys of *Six2^{Cre}Tet2^{f/f}* mice injected with cisplatin compared to the kidneys of *Six2^{Cre}* (control) mice injected with cisplatin (Fig. S8c,d). However, no observable changes in cell cycle progression were detected between doxorubicin-treated tubule cells from the kidneys of *Six2^{Cre}Tet2^{f/f}* mice and those from control mice (Fig. S8e).

We hypothesized that DNA damage repair might be impaired in the absence of TET2, which would lead to damaged DNA accumulation. DNA DSBs are repaired by HR and non-homologous end joining (dominant D-NHEJ or alternative Alt-NHEJ) (Fig. 5e)[40]. The protein level of phosphorylated BRCA1 (p-BRCA1) was lower in the doxorubicin-treated tubule cells isolated from *Six2^{Cre}Tet2^{f/f}* mice kidneys compared to those cells isolated from WT kidneys (Fig. 5d). We observed that the mRNA levels of HR pathway genes, including *BRCA2 DNA repair associated* (*Brca2*), *RAD51 recombinase* (*Rad51*), *X-ray repair cross complementing 2* (*Xrcc2*), and *Essential meiotic structure-specific endonuclease 1* (*Eme1*), was dramatically lower in PT cells of *Six2^{Cre}Tet2^{f/f}* mice compared to those in control PT cells from mice with UUO surgery (Fig. 5f). Similar changes were observed in bulk gene expression data from whole kidney lysates of *Six2^{Cre}Tet2^{f/f}* mice with UUO surgery (Fig. 5g). In line with the snRNA-seq results, *TET2* KD RPTEC showed lower expression of HR pathway genes (Fig. 5h, i). D-NHEJ and Alt-NHEJ pathway genes, including *DNA activated, catalytic polypeptide* (*Prkdc*), *X-ray repair cross complementing 5* (*Xrcc5*), *X-ray repair cross complementing 1* (*Xrcc6*), *DNA ligase 4* (*Lig4*), *Non-homologous end joining factor 1* (*Nhej1*), *Poly (ADP-ribose) polymerase 1* (*Parp1*), and *DNA ligase 3* (*Lig3*), were lower in PT cells of kidneys of *Six2^{Cre}Tet2^{f/f}* mice compared to kidneys obtained from control mice (Fig. S9a). However, we did not observe change in expression of these genes in kidneys of *Six2^{Cre}Tet2^{f/f}* mice following UUO injury (Fig. S9b, c) or in the *TET2* KD cells (Fig. S9d–g). PARP1 plays a key role in DNA damage repair. PARP inhibitors such as Olaparib has been recently introduced to the clinic[41]. We observed higher γH2AX level in tubule cells from the kidneys of *Six2^{Cre}Tet2^{f/f}* mice treated with both doxorubicin and the PARP inhibitor Olaparib, compared to those treated with doxorubicin alone (Fig. 5j). Furthermore, *Six2^{Cre}Tet2^{f/f}* mice injected with both cisplatin and Olaparib exhibited severe toxicity, leading to mortality by day 2 post-cisplatin injection (Fig. 5k, l). These results are consistent with the key role of *PARP* in DDR and repair after injury following *TET2* loss.

Amongst the genes that showed consistent changes in PT cells of *Six2^{Cre}Tet2^{f/f}* mice and RPTECs with *TET2* loss was the *INO80 complex ATPase subunit* (*INO80*) (Fig. 6b, c, and S10). *INO80* is known to play in DNA damage repair (both by HR and NHEJ pathways)[42–46]. Most importantly, we found that *INO80* is a kidney disease risk gene[8]. Kidney function genome wide association analysis showed a strong association between rs4924532 ($P = 1.31 \times 10^{-51}$) and kidney function (Fig. 6a). This GWAS SNP also showed a strong association of rs4924532 with *INO80* level in human kidney tubule sample ($P = 6.45 \times 10^{-6}$ in eQTL). *Ino80* expression was higher in PT cells of kidneys of mice with UUO
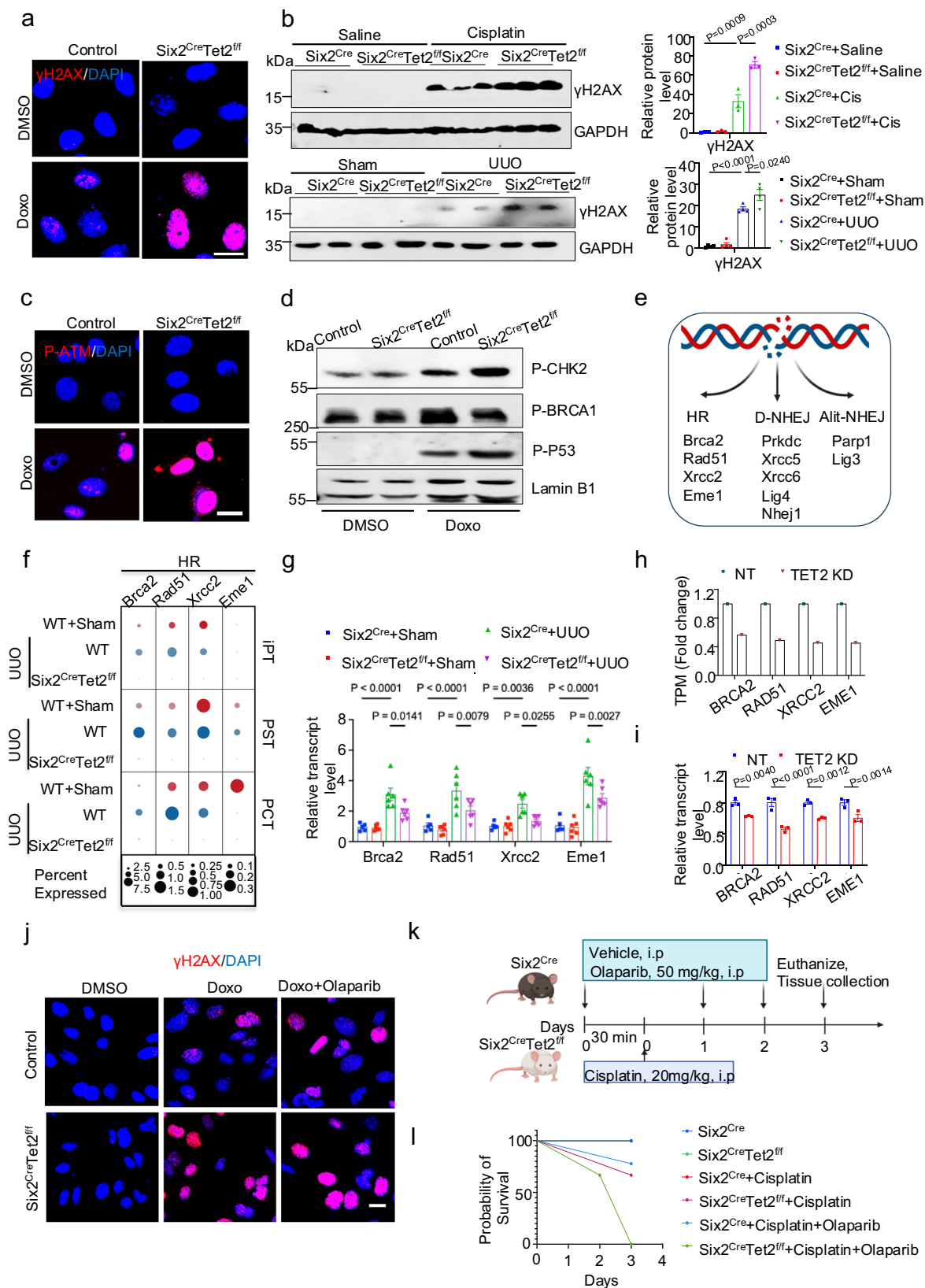
surgery or adenine diet (Fig. 6e, f). To further support the role of *INO80*, we found increased number of micronuclei in RTPEC following doxorubicin treatment with *INO80* knock-down, supporting the role of *INO80* in DDR (Fig. 6g, h).

In summary, these results indicate that *Tet2* loss causes accumulation of damaged DNA due to impaired DNA damage repair, and chromosome segregation defects in kidney tubule cells.

Fig. 5 | *Tet2* deficiency was associated with impaired DNA repair and accumulation of damaged DNA. a Representative images of immunofluorescence staining for γH2AX and DAPI in tubule cells from control and *Six2^{Cre}Tet2$^{f/f}$* mice treated with doxorubicin. *n* = 3 biological replicates per group. **b** Representative Western blots for γH2AX in kidney samples from control *Six2^{Cre}* and *Six2^{Cre}Tet2$^{f/f}$* mice injected with saline or cisplatin, or subjected to sham-operation or UUO surgery. (Right panel) Densitometric quantification of γH2AX normalized to GAPDH. Saline-injected or cisplatin-injected groups: *n* = 3 per group. Sham-operated or UUO-operated groups: *n* = 4 per group. **c** Representative immunofluorescence staining images for p-ATM in tubule cells from control and *Six2^{Cre}Tet2$^{f/f}$* mice treated with or without doxorubicin. *n* = 3 biological replicates per group. **d** Representative Western blots for nuclear p-CHK2, p-BRCA1, and p-p53 in tubule cells from *Six2^{Cre}* and *Six2^{Cre}Tet2$^{f/f}$* mice kidney treated with or without doxorubicin. Lamin B1 is the loading control. *n* = 3 biological replicates per group. **e** Double strand break (DSB) repair pathways. Created with BioRender.com. **f** Bubble plots showing expression of *Brca2, Rad51, Xrcc2*, and *Eme1* in PT clusters. Circle size shows percentage of positive cells, and color indicates gene expression. **g** Relative transcript levels of *BRCA2 DNA repair associated* (*Brca2*), *RAD51 recombinase* (*Rad51*), *X-ray repair cross complementing 2* (*Xrcc2*), and *Essential meiotic structure-specific endonuclease 1* (*Eme1*) in kidneys from *Six2^{Cre}* and *Six2^{Cre}Tet2$^{f/f}$* mice after sham-operation or UUO surgery. *Gapdh* was used for normalization. Sham-operated groups: *Six2^{Cre}* (*n* = 5), *Six2^{Cre}Tet2$^{f/f}$* (*n* = 6); UUO-operated groups: *n* = 6 per group. **h** Relative expression of *BRCA2, RAD51, XRCC2*, and *EME1* in control and *TET2*-knockdown RPTECs from RNA-seq analysis. **i** Relative transcript levels of *BRCA2, RAD51, XRCC2*, and *EME1* in control and *TET2*-knockdown RPTECs measured by qRT-PCR. *n* = 3 biological replicates per group. **j** Representative immunofluorescence images showing γH2AX staining in tubule cells from control and *Six2^{Cre}Tet2$^{f/f}$* mice treated with or without doxorubicin in the presence or absence of PARP inhibitor Olaparib. *n* = 3 biological replicates per group. **k** Experimental design: *Six2^{Cre}* and *Six2^{Cre}Tet2$^{f/f}$* mice injected with saline or cisplatin and in the presence or absence of Olaparib. Created with BioRender.com. **l** Survival curve for *Six2^{Cre}* and *Six2^{Cre}Tet2$^{f/f}$* mice injected with saline or cisplatin and supplemented with or without Olaparib. Saline-injected groups: *Six2^{Cre}* (*n* = 5), *Six2^{Cre}Tet2$^{f/f}$* (*n* = 4); Cisplatin-injected groups: *Six2^{Cre}* (*n* = 5), *Six2^{Cre}Tet2$^{f/f}$* (*n* = 6); Cisplatin and Olaparib-injected groups: *Six2^{Cre}* mice (*n* = 9) *Six2^{Cre}Tet2$^{f/f}$* mice (*n* = 6). Scale bar = 20 μm. Data are presented as mean ± SEM, analyzed using one-way ANOVA with Tukey's post hoc test (**b, g**) or a two-tailed unpaired Student's t-test (**h, i**). Source data are provided as a Source Data file.

Role of *cGAS-STING* activation in *Tet2* loss-induced kidney disease development

Cytosolic DNA (such as cytosolic micronuclei) is a strong activator of the cytosolic nucleotide sensors (cGAS/STING)[36,47]. We therefore wanted to understand whether cGAS/STING activation might mediate the deleterious effect of *TET2* loss. We found that cGAS-STING expression was higher in TET2 knockdown cells (Fig. 7a). Gene profiling by RNA sequencing showed that the expression of downstream STING target genes, including *Radical S-adenosyl methionine domain containing 2* (*RSAD2*), *2'-5'-oligoadenylate synthetase 1* (*OAS1*), *MX dynamin like GTPase 1* (*MX1*), *ISG20, IFIT1, IFIT2*, and *IFIT3*, was higher in the TET2 knockdown RPTECs (Fig. S11a), which was confirmed by qRT-PCR (Fig. 7b). The gene expression levels of the type I IFN response gene (Interferon *k, Ifnk*), interferon-stimulated genes (*Isg15, Mx1*, and *Oas1*), and the NF-kB target gene (*Il6*) were higher in *Six2^{Cre}Tet2$^{f/f}$* mice with UUO surgery compared to those in *Six2^{Cre}* mice with UUO surgery (Figs. 2h and S11b). Protein levels of cGAS, STING, phosphorylated TBK1 (p-TBK1), phosphorylated IRF3 (p-IRF3), and phosphorylated P65 (p-P65) was higher in cisplatin-injected *Six2^{Cre}Tet2$^{f/f}$* mice compared to cisplatin-treated control *Six2^{Cre}* mice (Fig. 7c and Fig. S11c). Immunofluorescence staining showed that p-STING level was higher in kidneys of *Six2^{Cre}Tet2$^{f/f}$* mice injected with cisplatin compared to those of *Six2^{Cre}* mice (Fig. S11d). In situ hybridization showed higher *Isg15* expression in kidneys of *Six2^{Cre}Tet2$^{f/f}$* mice injected with cisplatin when compared to those of control *Six2^{Cre}* mice injected with cisplatin (Fig. 7d). Similar results were obtained in the UUO model of kidney fibrosis (Figs. 7d and S11e).

To prove that cGAS-STING activation mediates kidney injury induced by tubule-specific loss of *Tet2*, we tested the effect of the STING inhibitor C176 in cisplatin-induced AKI mice (Fig. 7e). The expression of STING target genes, such as *Isg15*, was lower in kidneys of *Six2^{Cre}Tet2$^{f/f}$* mice treated with C176, indicating the effectiveness of the drug (Fig. S12). BUN levels, a marker kidney function, were lower in C176-treated mice compared to those in cisplatin-treated *Six2^{Cre}Tet2$^{f/f}$* mice (Fig. 7f). Histological examinations showed less severe kidney injury (such as dilated tubules and loss of brush border) in kidneys of *Six2^{Cre}Tet2$^{f/f}$* mice treated with both cisplatin and C176, compared to those treated with cisplatin alone (Fig. 7g). Levels of kidney injury markers, *Kim1* and *Ngal*, were lower in C176-injected animals (Fig. 7h).

To prove the role of cGAS and STING in TET2- mediated kidney injury, we used a genetic approach. We crossed *Six2^{Cre}Tet2$^{f/f}$* mice with *Cgas$^{f/f}$* mice or *Sting$^{f/f}$* mice (Fig. S13a) and then subjected these animals to UUO injury (Fig. S13b). Kidney protein levels of cGAS and STING confirmed the knockout efficiency of cGAS in *Six2^{Cre}Tet2$^{f/f}$Cgas$^{f/f}$* mice and STING in *Six2^{Cre}Tet2$^{f/f}$Sting$^{f/f}$* mice when compared to kidneys of

UUO subjected *Six2^{Cre}Tet2$^{f/f}$* mice (Fig. S13c). Histological analyses revealed reduced injury levels in the kidneys of *Six2^{Cre}Tet2$^{f/f}$Cgas$^{f/f}$* and *Six2^{Cre}Tet2$^{f/f}$Sting$^{f/f}$* mice subjected to UUO surgery, compared to *Six2^{Cre}Tet2$^{f/f}$* mice also undergoing UUO surgery (Fig. 7i). Sirius Red staining indicated less collagen accumulation in kidneys of UUO-subjected *Six2^{Cre}Tet2$^{f/f}$Cgas$^{f/f}$* mice and *Six2^{Cre}Tet2$^{f/f}$Sting$^{f/f}$* mice compared to those in *Six2^{Cre}Tet2$^{f/f}$* mice with UUO surgery (Figs. 7i and S13d). Transcript levels of fibrosis markers, including *Fibronectin1, Collagen1a1*, and *Collagen 3a1*, were lower in kidneys of UUO-subjected *Six2^{Cre}Tet2$^{f/f}$Cgas$^{f/f}$* and *Six2^{Cre}Tet2$^{f/f}$Sting$^{f/f}$* mice compared to those in *Six2^{Cre}Tet2$^{f/f}$* mice subjected to UUO (Fig. 7j). The protein level of fibronectin was lower in kidneys of UUO-subjected *Six2^{Cre}Tet2$^{f/f}$Cgas$^{f/f}$* and *Six2^{Cre}Tet2$^{f/f}$Sting$^{f/f}$* mice compared to those in *Six2^{Cre}Tet2$^{f/f}$* mice subjected to UUO (Fig. S13c).

In summary, these findings establish the critical role of the cGAS-STING in mediating *Tet2* loss-induced kidney injury and kidney disease development.

Discussion

Here, we demonstrate that *TET2* is a kidney disease risk gene using a multi-omics integration of kidney function GWAS fine mapping, human kidney meQTL and eQTL data, single-cell chromatin accessibility annotation, and CRISPR/Cas9-mediated genome editing. Mice and cells with genetic deletion of *TET2* in kidney tubule cells showed impaired DNA damage repair, resulting in the accumulation of cytosolic micronuclei, downstream cGAS-STING activation, and the development of kidney fibroinflammation.

TET2 is widely expressed in the body[48]. It is interesting to note that in the mouse and human kidneys *TET2* is almost exclusively expressed in the proximal tubule S3 segment. This is likely related to the presence of a PT/S3 specific enhancer region. The kidney function GWAS variants reside at this tubule enhancer and alter tubule specific *TET2* levels. Our study is the first to utilize mice with a kidney/tubule-specific deletion of *Tet2*, specifically exploring its role in the tubule cells, furthermore we show that the effect is not related to developmental programming as mice with conditional inducible deletion of TET2 in mature tubule cells showed the same phenotype, providing direct evidence of how germline genetic variations can alter *Tet2* levels in the kidney tubule. Mice with a global Tet2 deletion exhibited more severe acute renal injury following cisplatin injection[49] and ischemia-reperfusion injury[50]. The role of TET2 in diabetic kidney disease has been proposed, based on findings from cell culture studies[51].

Loss-of-function somatic mutations in TET2 within blood cell progenitors have recently gained major scientific interest, as they are
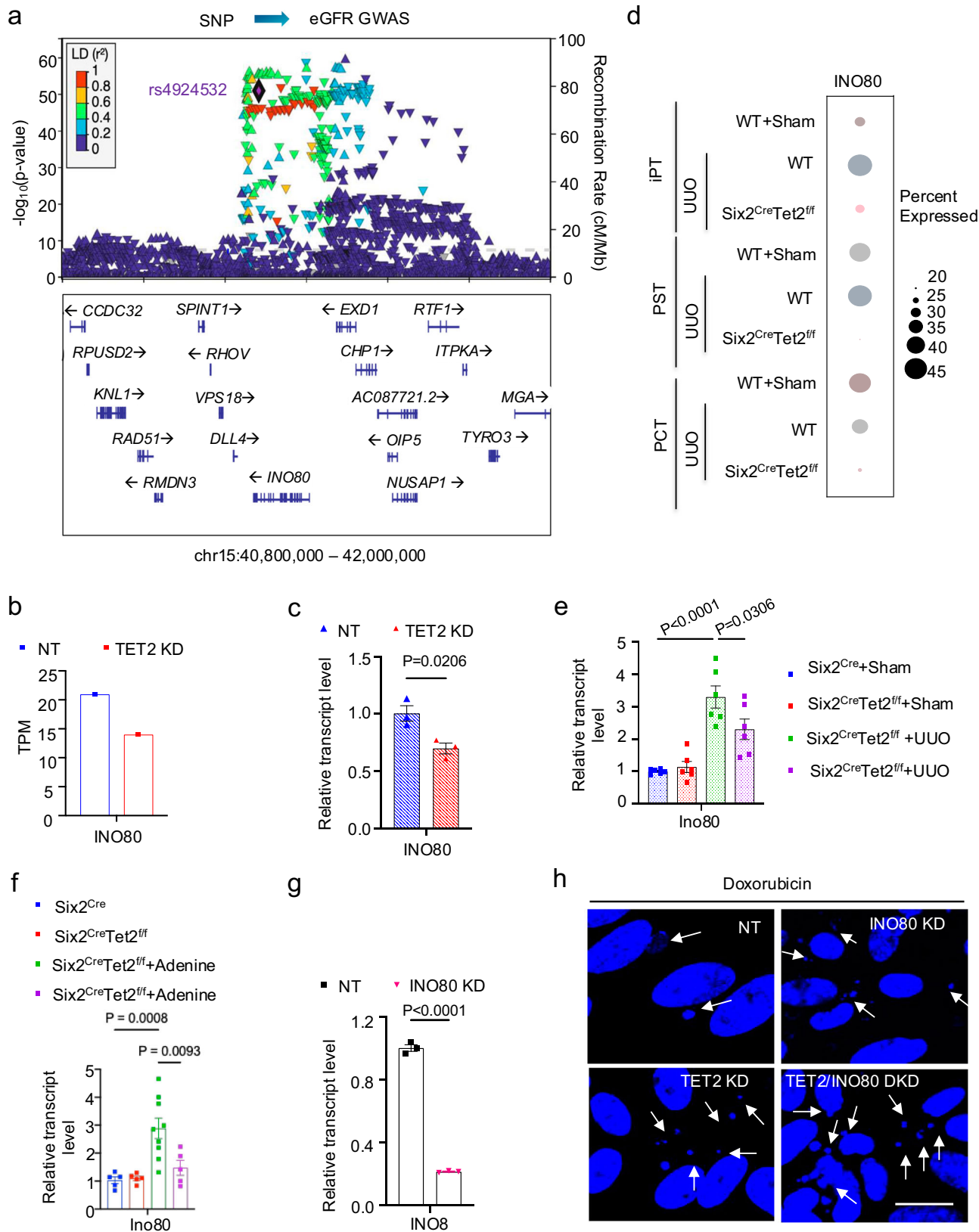
commonly observed in older individuals[52]. Clonal hematopoiesis of indeterminate potential (CHIP) is a common aging-related phenomenon in which early blood cell progenitors contribute to the formation of a genetically distinct subpopulation of blood cells[53]. Somatic mutations most commonly occur in *TET2* and *DNMT3A*[53]. CHIP was first reported to be associated with myeloid malignancies[54], but later

studies have uncovered the associations of CHIP with cardiovascular disease[55], melanoma progression[56], and Parkinson's disease[57]. The role of CHIP and somatic *TET2* mutations in kidney disease development has also been proposed[58,59]. Our studies suggest that germline regulatory genetic variants in *TET2* predispose individuals to kidney disease development. Future studies shall determine the role of CHIP and

Fig. 6 | Ino80 is another kidney disease risk gene associated with impaired DNA damage repair. a LocusZoom plot of GWAS (genotype and eGFRcrea association, *n* = 1,508,659 independent biological replicates). **b** RNA-seq of control and *TET2*-knockdown RPTECs showing *INO80* expression in these cells. **c**–**f** Relative transcript levels of *INO80* in control and *TET2*-knockdown RPTECs, and its levels in kidney samples from *Six2^Cre* and *Six2^CreTet2^f/f* mice subjected to sham-operation or UUO surgery or on control or adenine diets. For the control and *TET2*-knockdown (KD) RPTEC groups, *n* = 3 biological replicates per group. In the sham-operated and UUO-operated groups, *n* = 6 replicates per group. In the control diet-fed groups, *n* = 5 replicates per group. For the adenine diet-fed group, *Six2^Cre* mice had *n* = 9,

and *Six2^creTet2^f/f* mice had *n* = 5. **g** Relative transcript levels of *INO80* in *INO80* (CRISPR) knockdown cells compared to control RPTEC, with *n* = 3 biological replicates per group. **h** Representative images of immunofluorescence staining showing micronuclei (MN) in control, *INO80*-knockdown, *TET2*-knockdown, and *TET2* and *INO80* double knockdown RPTECs. *n* = 3 biological replicates per group. Scale bar = 20 µm. Data are presented as mean ± SEM and were analyzed by a two-tailed unpaired Student's t-test (**c,g**) or a one-way ANOVA followed by Tukey's post hoc test for multigroup comparison (**e,f**). Source data are provided as a Source Data file.

TET2 loss in blood cell progenitors, as well as the potential interaction between tubule cells and hematopoietic stem cells in kidney disease.

Our studies indicate the important role of TET2 in DNA damage repair, likely via the HR pathway in kidney disease development. The role of TET2 in DDR in leukemia cells has already been proposed[60]. TET2 has also been shown to localize to DSB in HeLa cells and human embryonic stem cells and proposed to be important for maintaining genomic integrity[61]. Future studies shall examine the exact molecular pathways regulated by TET2. Specifically, it will be important to understand whether its role in DDR is related to a non-enzymatic function of TET2 or potentially caused by DNA methylation changes of key genes involved in DDR. Our preliminary analysis indicates that TET2 effect is linked to its enzymatic function. First, we observed important differences in methylated cytosine levels between control, KO mice and those in a disease state (Fig. S13). Our prior studies indicated that *Tet2*, in conjunction with *Tet3*, markedly alters kidney development by interfering with the methylation of WNT pathway genes. Finally, we found that vitamin C, which can enhance the enzymatic activity of TET enzymes, ameliorated kidney disease development in mice with lower TET2 levels (Fig. S15).

Our studies indicate a broader role for DDR in kidney disease development beyond *TET2*. Our integrated GWAS and follow-up prioritization tool identified 57 kidney disease risk genes associated with DDR, including *BRCA2 and O-6-methylguanine-DNA methyltransferase (MGMT)*[8]. We identified *INO80* as another gene related to DNA repair and associated with kidney disease risk. The INO80 complex is a chromatin remodeling complex that regulates gene expression, DNA repair, and replication[42,45]. Aging is the strongest risk factor for kidney disease development; however, the exact mechanism of aging-associated kidney disease is poorly understood[62]. It is known that DNA methylation degrades with aging, and increased damage DNA accumulation and altered DDR are observed during aging[24]. Future studies shall establish the role of methylation changes and DDR in aging-associated kidney disease development.

Our studies indicate that the *Tet2* loss results in accumulation of micronuclei in tubule cells, activating the cGAS-STING pathway. We found that damaged DNA accumulating in injured kidney tubule cells leads to alterations in genes associated with chromosome segregation. The chromosome segregation defect is the likely cause of micronuclei accumulation. Cytosolic DNA, including micronuclei, has been shown to activate the cytosolic DNA sensors such as cGAS and STING[47]. To demonstrate the critical role of cGAS and STING in tubule cells, we generated mice with a tubule-specific genetic deletion of cGAS and STING. These mice showed protection from TET2-mediated kidney disease, indicating the critical role of this pathway in DDR alterations and kidney disease development. Finally, we show that pharmacological inhibition of STING protected mice from severe disease, indicating that STING inhibitors might be beneficial for patients with kidney disease specifically in patients carrying DDR pathway gene variants.

In conclusion, here we identify *TET2* as a kidney disease risk gene, which plays an important role in DNA damage repair, preventing altered chromosome segregation, cytosolic micronuclei accumulation, and cGAS-STING activation in kidney tubule cells.

Methods

Visualization of SNPs in GWAS, meQTL, and eQTL
LocusZoom was used to visualize genomic regions of interest on chromosome 4 for kidney function GWAS, meQTL, and eQTL of TET2 in whole kidneys or kidney tubules[8]. The meQTL box plot illustrates show the association between reference and alternative alleles of given genotypes and methylation level in kidney samples. The allele-specific expression (ASE) box plot was used to show the association between reference and alternative alleles of given genotypes and TET2 expression in tubule samples.

Bayesian colocalization analysis
As previously published[8], we performed Bayesian coloc analysis to identify the variants where the genotype effect on kidney function, methylation, and gene expression was shared. Bayesian coloc analysis was conducted using R package moloc (v0.1.0)[63] to estimate the posterior probability that an eGFR GWAS variant is associated with three traits (GWAS, meQTLs and eQTLs).

Animal studies
Mouse studies were approved by the Institutional Animal Care and Use Committee at the University of Pennsylvania. The *Tet2^f/f* (stock #017573), *Six2^Cre* (stock # 009606), *Pax8^rtTA* (stock #007176), TetO-Cre (*TRE^Cre*) (stock #00623), and *Sting^f/f* (stock #031670) mice were purchased from the Jackson Laboratory. *Cgas^f/f* mice were kindly provided by Prof. Charles Rice (Rockefeller University)[64]. *Tet2^f/f* was crossed with *Six2^Cre* mice to generate *Six2^CreTet2^f/f* mice. *Pax8^rtTA* and *TRE^Cre* mice were crossed with *Tet2^f/f* to generate *Pax8^rtTE^CreTet2^f/f* mice. *Cgas^f/f* and *Sting^f/f* were crossed with *Six2^CreTet2^f/f* mice to generate *Six2^CreTet2^f/f*Cgas ^f/f* mice and *Six2^CreTet2^f/* Sting ^f/f* mice, respectively. For the cisplatin injury model, 6-8-week-old mice were intraperitoneally injected with cisplatin (20 mg/kg; dissolved in 0.9% saline) and euthanized on day 3. For the unilateral ureteral obstruction model, 6-8-week-old mice underwent ligation of the left ureter and were euthanized on day 4. For adenine mouse disease model, 8-10-week-old mice were given a control (0.6% calcium and 0.9% phosphorus adjusted diet) or an adenine (0.2% adenine, 0.6% calcium and 0.9% phosphorus) diet and euthanized 4 weeks after starting the adenine food. In the PARP inhibition experiment, Olaparib (50 mg/kg; Tocris Bioscience™, #75-791-0) was administered intraperitoneally 30 minutes prior to cisplatin injection, with subsequent daily administrations following cisplatin injection. In the STING pharmacological inhibition experiment, C176 (750 nm per mouse, Bio Vision, #B2341) or DMSO dissolved in 85 µl corn oil was administered intraperitoneally. This administration occurred at 2 h, 24 h, and 48 h before the injection of cisplatin (20 mg/kg) or saline, and then daily after cisplatin injection. All mice were provided food and water ad libitum and monitored daily.

Single nucleus RNA sequencing
Nuclei were extracted from flash-frozen kidney tissue. Briefly, 10-30 mg of frozen kidney tissue were minced on ice into pieces in lysis
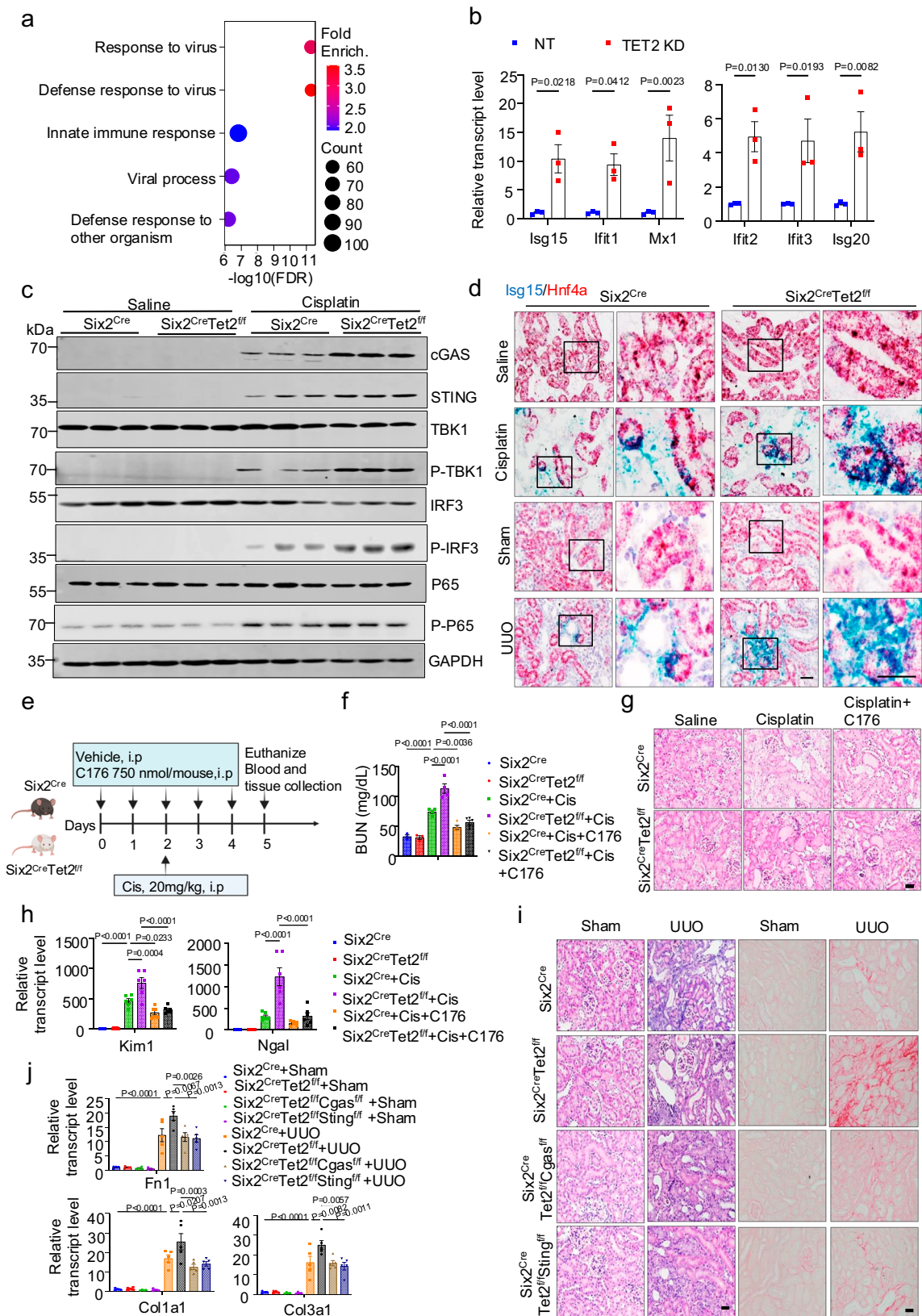
buffer (Tris-HC, NaCl, MgCl2, NP40, and RNAse inhibitor), transferred into a gentleMACS C tube, and homogenized using gentleMACS homogenizer. Next, the homogenized tissue was filtered through a 40 μm strainer (Fisher Scientific, #08-771-1) and then centrifuged at 500 × g for 5 mins at 4 °C. The pellet was resuspended in wash buffer (BSA, RNAse inhibitor, 1× PBS) and then filtered through a 40 μm Flowmi cell strainer (Sigma Aldrich, #BAH136800040-50EA). After checking for nuclear quality and counting, 30,000 cells were loaded into the 10X Chromium Controller (PN-120223). The cDNA libraries were constructed using the 10X Chromium library construction kit (PN-1000190). Libraries were subjected to quality control using the Agilent Bioanalyzer High Sensitivity DNA kit (Agilent Technologies, 5067-

Fig. 7 | cGAS and STING mediate the *TET2*-loss induced kidney damage. a GO functional analysis of genes upregulated (1.5-fold) in *TET2*-knockdown RPTECs compared to controls. Significantly biological process GO terms ($p < 0.05$) are presented, with *p*-values as negative log10-transformed. **b** Relative transcript levels of *Isg15, Ifit1, Ifit2, Ifit3, Mx1*, and *Isg20* in control and *TET2* knockdown RPTECs. $n = 3$ biological replicates per group. **c** Representative Western blots for *cGAS, STING, TBK1, p-TBK1, IRF3, p-IRF3, P65*, and phosphorylated p65 (p-p65) in kidney samples from *Six2^Cre^* and *Six2^Cre^Tet2^f/f^* mice subjected to sham operation or UUO surgery. $n = 3$ per group. **d** Representative in situ hybridization images of *Isg15* (blue) and *Hnf4a* (red) in kidney sections from *Six2^Cre^* and *Six2^Cre^Tet2^f/f^* mice injected with saline or cisplatin, or subjected to sham-operation or UUO surgery. **e** Experimental design: *Six2^Cre^* and *Six2^Cre^Tet2^f/f^* mice injected with saline or cisplatin in the presence or absence of the STING inhibitor C176. Created with BioRender.com. **f** Serum BUN levels in *Six2^Cre^* and *Six2^Cre^Tet2^f/f^* mice injected with saline or cisplatin either in the presence or absence of C176. Saline-injected groups: $n = 3$ biological replicates per group; Cisplatin-injected groups: $n = 4$ biological replicates per group; Cisplatin

and C176-injected groups: *Six2^Cre^* ($n = 4$) and *Six2^Cre^Tet2^f/f^* ($n = 5$). **g** Representative images of H&E-stained kidney sections from *Six2^Cre^* and *Six2^Cre^Tet2^f/f^* mice injected with saline or cisplatin either in the presence or absence of C176. **h** Relative transcript levels of *Kim1* and *Ngal* in kidneys from *Six2^Cre^* and *Six2^Cre^Tet2^f/f^* mice injected with saline or cisplatin, with or without C176. Saline-injected groups: $n = 5$ samples per group. Cisplatin-injected groups: $n = 6$ samples per group. Cisplatin and C176-treated groups: $n = 6$ samples per group. **i** Representative images of H&E-stained and Sirius Red-stained kidney sections from *Six2^Cre^*, *Six2^Cre^Tet2^f/f^*, *Six2^Cre^Tet2^f/f^Cgas^f/f^*, and *Six2^Cre^Tet2^f/f^Sting^f/f^* mice subjected to sham-operation or UUO surgery. **j** Relative transcript levels of *Fn1, Col1a1*, and *Col3a1* in kidneys from *Six2^Cre^*, *Six2^Cre^Tet2^f/f^*, *Six2^Cre^Tet2^f/f^Cgas^f/f^*, and *Six2^Cre^Tet2^f/f^Sting^f/f^* mice after sham-operation or UUO surgery. Sham-operated groups: $n = 4$; UUO-operated groups: $n = 5$. Scale bar = 20 μm. Data are presented as mean ± SEM and were analyzed using a two-tailed unpaired Student's t-test (**b**) or a one-way ANOVA followed by Tukey's post hoc test for multigroup comparison (**f**, **h**, **j**). Data are representative of three independent experiments (**d**, **g**, **i**). Source data are provided as a Source Data file.

4626). The following demultiplexing was used to sequence libraries using the Illumina Novaseq 6000 system with 2 × 150 paired-end kits: 28 bp Read1 for cell barcode and UMI, 10 bp i7 index, 10 bp i5 index, and 90 bp Read2 for transcript.

Cell culture and lentiviral production
Primary tubular epithelial cells were isolated from the kidneys of 3-4-week-old mice. Briefly, kidneys were minced into pieces and digested in RPMI 1640 medium (Gibco, #21875-034) containing collagenase I (2 mg/ml, Sigma Aldrich) for 30 min at 37 °C. Next, fetal bovine serum (FBS) was used to deactivate collagenase I activity and cells were sequentially sieved through 100, 70, and 40 μm mesh. After removing red blood cells, the tubules cells were cultured in RPMI 1640 supplemented with 10% FBS, rhEGF (20 ng/ml), 1× insulin-transferrin-selenium (ITS), and 1% penicillin-streptomycin.

Immortalized human RPTECs (ATCC; CRL-4031) were cultured in Dulbecco's modified Eagle's medium (DMEM)-F12, supplemented with hydrocortisone (25 ng/ml), ascorbic acid (3.5 μg/ml), sodium selenite (8.65 ng/ml), transferrin (5.0 μg/ml), insulin (5.0 μg/ml), triiodo-L-thyronine (5 pM), prostaglandin E1 (25 ng/ml), rhEGF (10 ng/ml), sodium bicarbonate (1.2 mg/ml), 1% penicillin-streptomycin, and G418 (0.1 mg/ml).

For the cytosolic micronuclei analysis experiments, the primary epithelial tubule cells or RPTECs were exposed to doxorubicin (1 μM) for 25 mins. For the DNA damage analysis experiments, the primary epithelial tubule cells or RPTECs were exposed to doxorubicin (1 μM) for 25 mins and analyzed after 8 h. For the cell cycle analysis and DDR analysis experiments, the primary epithelial tubule cells were treated with doxorubicin (1 μM) for 24 h. For the PARP inhibition experiment, cells were exposed to Olaparib (1 μM) for 1 h and then treated with or without doxorubicin (1 μM) for 8 h.

Human embryonic kidney (HEK) 293 T (HEK293T) cells (ATCC, #CRL-3216) were used for packaging lentivirus. The cells were cultured in DMEM (Mediatech, #MT10-013-CV) supplemented with 10% FBS and 1% penicillin-streptomycin and maintained in a humidified 5% CO_2 atmosphere at 37 °C.

For lentivirus production, HEK293T cells were transfected with the plasmid of interest, along with the lentiviral packing and envelope plasmids, pPAX2 (Addgene, #12260, a gift from Didier Trono) and pMD2.G (Addgene, #12259, a gift from Didier Trono), using polyethylenimine (PEI, Biotechne, #7854).

Cell line generation
CRISPRi RPTEC cells were generated by stably transducing RPTECs with lentivirus expressing ZIM3 KRAB-dCas9-mCherry under the UCOE-SFFV promoter. Cells stably expressing mCherry were sorted using fluorescence-activated cell sorting. The

plasmid pHR-UCOE-SFFV-dCas9-mCherry-ZIM3-KRAB was a gift from Mikko Taipale (Addgene plasmid #154473). The CRISPRi RPTEC cell line was verified by monitoring mCherry fluorescence over several generations.

CRISPR/Cas9 mediated genomic region deletion
All annealed sgRNA oligos were subcloned into a Cas9 expression plasmid (lentiCRISPR v2, Addgene, #52961, a gift from Feng Zhang) with the Bsmb1 site. All constructs were verified by Sanger sequencing.

Lentivirus was prepared as previously described. Lentivirus-containing supernatants supplemented with polybrene (Santa Cruz Biotechnology, #sc-134220) were used for lentiviral transduction for the human RPTEC. After 72 h, cells were harvested, and *TET2* and *PPA2* expression was determined by qRT-PCR. At the same time, DNA was isolated, and sgRNAs target region deletion were determined by Sanger sequencing. sgRNA sequences are listed in Supplementary Data 3, and PCR primer sequences are listed in Supplementary Data 4.

CRISPR interference
The sgRNA expressing plasmids were generated as previously published[65]. Briefly, annealed sgRNA oligos were subcloned into LRG2.1 (Addgene #108098, a gift from Christopher Vakoc) with the Bsmb1 site. All constructs were verified by Sanger sequencing. The sgRNA sequences used in this study are in Supplementary Data 3.

Lentivirus was prepared as previously described. The lentivirus-containing supernatants, supplemented with polybrene, were immediately used for lentiviral transduction of human RPTEC stable expressing dCas9-KRAB-ZIM3.

Human RPTEC RNA Sequencing
RNA was extracted using the RNeasy Mini Kit (Qiagen, Cat# 74106). After quality assessment by Agilent Bioanalyzer 2100, RNA-Seq libraries were generated using the TruSeq RNA Sample Prep Kit (Illumina, San Diego, CA). Low-quality bases were trimmed using Trimgalore, and RNA-seq reads were aligned to the human genome (hg19) using STAR (v2.6.1a) based on GENCODE v29 annotations. RSEM (v1.3.1) was used to quantify gene-level read counts and expressed as transcripts per million (TPM).

RNA extraction and qRT-PCR
RNA was isolated using Trizol reagent (Invitrogen) and was transcribed into cDNA using cDNA Reverse Transcription Kit (Applied Biosystems, Cat. #4368813). qRT-PCR was performed using the SYBR Green Master Mix (Applied Biosystems, Cat. #A25742-PEC). The data were normalized and analyzed using the 2-ΔΔCt method with indicated reference gene. Primer sequences are provided in Supplementary Data 5.

Western blot

Kidney tissue or cultured cells were homogenized in lysis buffer and were separated by SDS-PAGE and then transferred to PVDF membranes. Transferred blots were blocked for 1 h in 5% non-fat milk or 5% BSA in Tris-buffered saline. Membranes were incubated with specific primary antibodies at 4 °C overnight, followed by incubation with a horseradish peroxidase-conjugated anti-mouse antibody (1:5,000), or anti-rabbit antibody (1:5,000), or IR-conjugated anti-mouse antibody (1:20,000), and anti-rabbit (1:20,000) antibody at room temperature for 1 h. The signal was developed with Immobilon forte western HRP substrate (Millipore, #WBKLS0500) using Odyssey®Fc Imaging System (LICOR) equipment and measured with Iamge Studio Lite software. The antibodies used in the study are listed in Supplementary Data 6.

Histological analysis

Kidneys were fixed in 10% neutral formalin. Paraffin-embedded sections were stained with hematoxylin and eosin (H&E). Sirius Red staining was performed to determine the degree of fibrosis. In situ hybridization was performed using paraffin-embedded kidney tissue samples and the RNAscope 2.5 HD Duplex Detection Kit (bio-techne, Cat. #322436) following manufacturers' original protocol. The following probes were used for the RNAscope assay: Mm-*Tet2* (bio-techne, Cat. # 511591), Mm-I*sg15* (bio-techne, Cat# 559271-O1), Mm-*Hnf4a* (bio-techne, Cat# 497651-C2). Immunofluorescence analyzes were performed on paraformaldehyde-fixed cells and formalin-fixed, paraffin-embedded kidney sections. To visualize the expression of proteins in the kidney, paraffin-embedded sections were deparaffinized, rehydrated, and incubated with indicated primary antibodies. Slides were incubated with fluorescent-conjugated secondary antibodies, counterstained and mounted with DAPI for nuclear staining. To visualize the protein expression in the paraformaldehyde-fixed cells, we permeabilized the cells with 0.2% Triton X 100, blocked with 3% BSA, then incubated with indicated primary antibodies and fluorescent conjugated secondary antibodies, and counterstained with DAPI.

BUN and creatinine level

Blood urea nitrogen levels (BUN) was measured using Infinity™ Urea Liquid Stable Reagent (Pointe Scientific, #B7552150). Serum creatinine was detected by Creatinine Enzymatic and Creatinine Standard (DIAZYME #DZ072B-KY1). Both measurements were performed following the manufacturers' instructions.

Fluorescence-activated cell sorting analysis for cell cycle distribution

Cells were prepared for propidium iodide (Sigma) staining following standard protocols. DNA content was then analyzed using a CytoFLEX Analyzer.

Bioinformatic analysis for single-nucleus RNA sequencing data

We generated a gene-by-cell count matrix by aligning its fastq files to the mm10 reference dataset using 10X Genomics Cell Ranger ARC v2.0.2). The quality control (QC) included removing ambient mRNA contamination, eliminating low-quality cells and genes, and excluding doublet-like cells. We used "SoupX" to remove ambient mRNA. We defined low-quality cells as those with the following criteria: unique molecular identifiers (UMI) ≤ 500 or ≥ 10,000, the number of detected genes ≤300 or ≥ 3000, the percentage of mitochondrially encoded genes reads > 1%, and complex ≥ 0.25. We further removed genes that were expressed in < 10 cells. "DoubletFinder" was used to exclude doublet-like cells. To process the data, we used Seurat 4.0.4.

The data were normalized and scaled using the NormalizeData() and ScaleData() functions in Seurat, and variable features were identified with FindVariableFeatures(). Cluster identities were assigned using expression of known marker genes[34]. Differentially expressed genes (DEGs) in each cluster were determined using the FindAllMarkers() function with the "*MAST*" test for transcripts present in at least 10% of cells with an absolute log2-fold-change (log2FC) threshold of 0.25. A Bonferroni adjusted *P*-value (*P*-adj) < 0.05 was considered statistically significant.

Quantification and statistical analysis

Statistical analyses were performed using GraphPad Prism software (GraphPad Software Inc., La Jolla, CA). An unpaired, two-tailed Student's t-test was used to compare two groups. One-way ANOVA was used to compare multiple groups, followed by Tukey's post hoc test. $p < 0.05$ was considered significant. All data are shown as mean ± SEM.

Study approval

The University of Pennsylvania institutional review board (IRB) approved the human kidney sample collection. We engaged with an external honest broker who was responsible for human kidney sample collection. No personal data were acquired.

Reporting summary

Further information on research design is available in the Nature Portfolio Reporting Summary linked to this article.

Data availability

Mouse snRNA-seq data and RNA sequencing data generated in this study have been deposited in the GEO under accession code: GSE273027. The kidney meQTLs, kidney eQTLs, human kidney snATAC-seq data, and snRNA-seq data used in this study are available in the GEO under accession codes: GSE115098, GSE173343, GSE172008, GSE200547, and GSE211785 and are publicly available online at the Susztaklab Kidney Biobank (http://www.susztaklab.com/Kidney_meQTL/index.php; http://www.susztaklab.com/Kidney_eQTL/index.php). The adult human kidney histone modifications (H3K4me3 and H3K27ac) by ChIP-seq used in this study are available in the GEO under accession codes: GSM621648 and GSM1112806. Chromatin states for human adult kidneys were generated using ChromHMM (v1.17), by training a 15-state model to capture all the key interactions between the chromatin marks as previously published[8]. The data for the eGFRcrea GWAS and kidney tubule ASE used in this study are unpublished (Liu et al. in Revision, https://susztaklab.com/GWAS2M/GWAS.php). Additional details on protocols and special reagents used in this study are provided upon request from the corresponding author. Source data are provided with this paper.

References

1. Jager, K. J. et al. A single number for advocacy and communication-worldwide more than 850 million individuals have kidney diseases. *Nephrol. Dial. Transpl.* **34**, 1803–1805 (2019).
2. Kovesdy, C. P. Epidemiology of chronic kidney disease: an update 2022. *Kidney Int Suppl.* **12**, 7–11 (2022).
3. Collaboration, G. B. D. C. K. D. Global, regional, and national burden of chronic kidney disease, 1990-2017: a systematic analysis for the Global Burden of Disease Study 2017. *Lancet* **395**, 709–733 (2020).
4. Ko, Y. A. et al. Genetic-variation-driven gene-expression changes highlight genes with important functions for kidney disease. *Am. J. Hum. Genet* **100**, 940–953 (2017).
5. Wuttke, M. et al. A catalog of genetic loci associated with kidney function from analyses of a million individuals. *Nat. Genet* **51**, 957–972 (2019).
6. Hirohama, D. & Susztak, K. From mapping kidney function to mechanism and prediction. *Nat. Rev. Nephrol.* **18**, 76–77 (2022).
7. Stanzick, K. J. et al. Discovery and prioritization of variants and genes for kidney function in >1.2 million individuals. *Nat. Commun.* **12**, 4350 (2021).

8. Liu, H. et al. Epigenomic and transcriptomic analyses define core cell types, genes and targetable mechanisms for kidney disease. *Nat. Genet* **54**, 950–962 (2022).

9. Sullivan, K. M. & Susztak, K. Unravelling the complex genetics of common kidney diseases: from variants to mechanisms. *Nat. Rev. Nephrol.* **16**, 628–640 (2020).

10. Zhu, Q. et al. Prioritizing genetic variants for causality on the basis of preferential linkage disequilibrium. *Am. J. Hum. Genet* **91**, 422–434 (2012).

11. Consortium, G. T. Human genomics. The Genotype-Tissue Expression (GTEx) pilot analysis: multitissue gene regulation in humans. *Science* **348**, 648–660 (2015).

12. Qiu, C. et al. Renal compartment-specific genetic variation analyses identify new pathways in chronic kidney disease. *Nat. Med* **24**, 1721–1731 (2018).

13. Sheng, X. et al. Mapping the genetic architecture of human traits to cell types in the kidney identifies mechanisms of disease and potential treatments. *Nat. Genet* **53**, 1322–1333 (2021).

14. Moore, L. D., Le, T. & Fan, G. DNA methylation and its basic function. *Neuropsychopharmacology* **38**, 23–38 (2013).

15. Ito, S. et al. Role of Tet proteins in 5mC to 5hmC conversion, ES-cell self-renewal and inner cell mass specification. *Nature* **466**, 1129–1133 (2010).

16. Ito, S. et al. Tet proteins can convert 5-methylcytosine to 5-formylcytosine and 5-carboxylcytosine. *Science* **333**, 1300–1303 (2011).

17. Sriraman, A., Debnath, T. K., Xhemalce, B. & Miller, K. M. Making it or breaking it: DNA methylation and genome integrity. *Essays Biochem* **64**, 687–703 (2020).

18. Jones, P. A. & Takai, D. The role of DNA methylation in mammalian epigenetics. *Science* **293**, 1068–1070 (2001).

19. Li, S. Y. et al. DNMT1 in Six2 Progenitor Cells Is Essential for Transposable Element Silencing and Kidney Development. *J. Am. Soc. Nephrol.* **30**, 594–609 (2019).

20. Guan, Y. et al. Dnmt3a and Dnmt3b-decommissioned fetal enhancers are linked to kidney disease. *J. Am. Soc. Nephrol.* **31**, 765–782 (2020).

21. Yan, Y. et al. Unraveling the epigenetic code: human kidney DNA methylation and chromatin dynamics in renal disease development. *Nat. Commun.* **15**, 873 (2024).

22. Chatterjee, N. & Walker, G. C. Mechanisms of DNA damage, repair, and mutagenesis. *Environ. Mol. Mutagen* **58**, 235–263 (2017).

23. Sun, S., Osterman, M. D. & Li, M. Tissue specificity of DNA damage response and tumorigenesis. *Cancer Biol. Med* **16**, 396–414 (2019).

24. Hayashi, K., Hishikawa, A. & Itoh, H. DNA damage repair and DNA methylation in the kidney. *Am. J. Nephrol.* **50**, 81–91 (2019).

25. Selfridge, J., Hsia, K. T., Redhead, N. J. & Melton, D. W. Correction of liver dysfunction in DNA repair-deficient mice with an ERCC1 transgene. *Nucleic Acids Res* **29**, 4541–4550 (2001).

26. Soto-Palma, C., Niedernhofer, L. J., Faulk, C. D. & Dong, X. Epigenetics, DNA damage, and aging. *J Clin Invest* **132** (2022).

27. Morris, A. P. et al. Trans-ethnic kidney function association study reveals putative causal genes and effects on kidney-specific disease aetiologies. *Nat. Commun.* **10**, 29 (2019).

28. Graham, S. E. et al. Sex-specific and pleiotropic effects underlying kidney function identified from GWAS meta-analysis. *Nat. Commun.* **10**, 1847 (2019).

29. Hellwege, J. N. et al. Mapping eGFR loci to the renal transcriptome and phenome in the VA Million Veteran Program. *Nat. Commun.* **10**, 3842 (2019).

30. Gazal, S. et al. Combining SNP-to-gene linking strategies to identify disease genes and assess disease omnigenicity. *Nat. Genet* **54**, 827–836 (2022).

31. Gate, R. E. et al. Genetic determinants of co-accessible chromatin regions in activated T cells across humans. *Nat. Genet* **50**, 1140–1150 (2018).

32. Liang, X. et al. Tet2- and Tet3- mediated cytosine hydroxymethylation in six2 progenitor cells in mice is critical for nephron progenitor differentiation and nephron endowment. *J. Am. Soc. Nephrol.* **34**, 572–589 (2023).

33. Kobayashi, A. et al. Six2 defines and regulates a multipotent self-renewing nephron progenitor population throughout mammalian kidney development. *Cell Stem Cell* **3**, 169–181 (2008).

34. Park, J. et al. Single-cell transcriptomics of the mouse kidney reveals potential cellular targets of kidney disease. *Science* **360**, 758–763 (2018).

35. Bakhoum, S. F., Kabeche, L., Murnane, J. P., Zaki, B. I. & Compton, D. A. DNA-damage response during mitosis induces whole-chromosome missegregation. *Cancer Discov.* **4**, 1281–1289 (2014).

36. Krupina, K., Goginashvili, A. & Cleveland, D. W. Causes and consequences of micronuclei. *Curr. Opin. Cell Biol.* **70**, 91–99 (2021).

37. He, B. et al. Chromosomes missegregated into micronuclei contribute to chromosomal instability by missegregating at the next division. *Oncotarget* **10**, 2660–2674 (2019).

38. Mehta, A. & Haber, J. E. Sources of DNA double-strand breaks and models of recombinational DNA repair. *Cold Spring Harb. Perspect. Biol.* **6**, a016428 (2014).

39. Novais-Cruz, M. et al. Mitotic DNA damage promotes chromokinesin-mediated missegregation of polar chromosomes in cancer cells. *Mol. Biol. Cell* **34**, ar47 (2023).

40. Shibata, A. & Jeggo, P. A. DNA double-strand break repair in a cellular context. *Clin. Oncol. (R. Coll. Radio.)* **26**, 243–249 (2014).

41. Dias, M. P., Moser, S. C., Ganesan, S. & Jonkers, J. Understanding and overcoming resistance to PARP inhibitors in cancer therapy. *Nat. Rev. Clin. Oncol.* **18**, 773–791 (2021).

42. Morrison, A. J. et al. INO80 and gamma-H2AX interaction links ATP-dependent chromatin remodeling to DNA damage repair. *Cell* **119**, 767–775 (2004).

43. Tsukuda, T., Fleming, A. B., Nickoloff, J. A. & Osley, M. A. Chromatin remodelling at a DNA double-strand break site in Saccharomyces cerevisiae. *Nature* **438**, 379–383 (2005).

44. van Attikum, H., Fritsch, O. & Gasser, S. M. Distinct roles for SWR1 and INO80 chromatin remodeling complexes at chromosomal double-strand breaks. *EMBO J.* **26**, 4113–4125 (2007).

45. van Attikum, H., Fritsch, O., Hohn, B. & Gasser, S. M. Recruitment of the INO80 complex by H2A phosphorylation links ATP-dependent chromatin remodeling with DNA double-strand break repair. *Cell* **119**, 777–788 (2004).

46. Gospodinov, A. et al. Mammalian Ino80 mediates double-strand break repair through its role in DNA end strand resection. *Mol. Cell Biol.* **31**, 4735–4745 (2011).

47. Mackenzie, K. J. et al. cGAS surveillance of micronuclei links genome instability to innate immunity. *Nature* **548**, 461–465 (2017).

48. Rasmussen, K. D. & Helin, K. Role of TET enzymes in DNA methylation, development, and cancer. *Genes Dev.* **30**, 733–750 (2016).

49. Bao, Y. et al. DNA demethylase Tet2 suppresses cisplatin-induced acute kidney injury. *Cell Death Discov.* **7**, 167 (2021).

50. Yan, H. et al. Ten-eleven translocation methyl-cytosine dioxygenase 2 deficiency exacerbates renal ischemia-reperfusion injury. *Clin. Epigenetics* **12**, 98 (2020).

51. Yang, L. et al. Effect of TET2 on the pathogenesis of diabetic nephropathy through activation of transforming growth factor beta1 expression via DNA demethylation. *Life Sci.* **207**, 127–137 (2018).

52. Ferrone, C. K., Blydt-Hansen, M. & Rauh, M. J. Age-Associated TET2 Mutations: Common Drivers of Myeloid Dysfunction, Cancer and Cardiovascular Disease. *Int J Mol Sci* **21** (2020).

53. Kessler, M. D. et al. Common and rare variant associations with clonal haematopoiesis phenotypes. *Nature* **612**, 301–309 (2022).

54. Delhommeau, F. et al. Mutation in TET2 in myeloid cancers. *N. Engl. J. Med* **360**, 2289–2301 (2009).

55. Ostriker, A. C. et al. TET2 protects against vascular smooth muscle cell apoptosis and intimal thickening in transplant vasculopathy. *Circulation* **144**, 455–470 (2021).

56. Pan, W. et al. The DNA methylcytosine dioxygenase Tet2 sustains immunosuppressive function of tumor-infiltrating myeloid cells to promote melanoma progression. *Immunity* **47**, 284–297.e285 (2017).

57. Marshall, L. L. et al. Epigenomic analysis of Parkinson's disease neurons identifies Tet2 loss as neuroprotective. *Nat. Neurosci.* **23**, 1203–1214 (2020).

58. Vlasschaert, C. et al. Association of clonal hematopoiesis of indeterminate potential with worse kidney function and anemia in two cohorts of patients with advanced chronic kidney disease. *J. Am. Soc. Nephrol.* **33**, 985–995 (2022).

59. Sano, S. et al. CRISPR-mediated gene editing to assess the roles of tet2 and dnmt3a in clonal hematopoiesis and cardiovascular disease. *Circ. Res* **123**, 335–341 (2018).

60. Maifrede, S. et al. TET2 and DNMT3A mutations exert divergent effects on dna repair and sensitivity of leukemia cells to PARP inhibitors. *Cancer Res* **81**, 5089–5101 (2021).

61. Kafer, G. R. et al. 5-hydroxymethylcytosine marks sites of DNA damage and promotes genome stability. *Cell Rep.* **14**, 1283–1292 (2016).

62. Kazancioglu, R. Risk factors for chronic kidney disease: an update. *Kidney Int Suppl.* **3**, 368–371 (2013).

63. Giambartolomei, C. et al. A Bayesian framework for multiple trait colocalization from summary association statistics. *Bioinformatics* **34**, 2538–2545 (2018).

64. Schoggins, J. W. et al. Pan-viral specificity of IFN-induced genes reveals new roles for cGAS in innate immunity. *Nature* **505**, 691–695 (2014).

65. Cao, Z. et al. ZMYND8-regulated IRF8 transcription axis is an acute myeloid leukemia dependency. *Mol. Cell* **81**, 3604–3622.e3610 (2021).

Acknowledgements

Author contributions

This study was led by K.S. K.S. and X.L. designed the study, analyzed the data, and wrote the manuscript with input from other authors. X.L., A.A., and A.N. performed experiments. H.L., H.H., X.L., E.H., J.Z., and K.K. performed computational analysis.

Competing interests

Additional information

Supplementary information The online version contains supplementary material available at https://doi.org/10.1038/s41467-024-53798-x.

Correspondence and requests for materials should be addressed to Katalin Susztak.

Peer review information *Nature Communications* thanks Michael Eadon, Vishal Patel and the other, anonymous, reviewer for their contribution to the peer review of this work. A peer review file is available.

Reprints and permissions information is available at http://www.nature.com/reprints

Publisher's note Springer Nature remains neutral with regard to jurisdictional claims in published maps and institutional affiliations.